Experimental study on spatial prefabricated self-centering steel frame with beam-column connections containing bolted web friction devices

Yanxia Zhang[a,*], Quangang Li[b], Yan Zhuge[c], Anran Liu[b], Wenzhan Zhao[b]

[a] Beijing Advanced Innovation Center for Future Urban Design, Beijing University of Civil Engineering and Architecture, 100044, PR China
[b] School of Civil and Transportation Engineering, Beijing University of Civil Engineering and Architecture, 100044, PR China
[c] School of Natural & Built Environments, University of South Australia, SA 5000, Australia

ABSTRACT

The structural system of prefabricated self-centering steel frame (PSCF) was proposed previously by the author. Experimental studies focusing on PSCF connections, plane frame, overall structures as well as the numerical simulations were conducted. Compared with the self-centering steel frame (SCF), the PSCF has avoided the on-site aerial tension of steel strands and simultaneously achieves similar seismic performance as well as self-centering capacity. While the self-centering function of both PSCF and SCF may be restrained by conventional floor systems. Based on this thesis, a spatial PSCF with a new type of floor system containing sliding secondary beams was proposed in this paper to enable the frame expansion, and pseudo-dynamic and quasi-static tests toward it were conducted. The test results indicated that the proposed new floor system was reliable and feasible in accommodating the frame expansion. Meanwhile, the spatial PSCF with the new floor system has a favorable self-centering capacity, reliable gap-opening mechanism, superior seismic performance and enough redundancy to withstand multiple aftershocks.

1. Introduction

Self-centering steel frames (SCFs) can mitigate structural damage, reduce or eliminate residual deformation and are easy to repair after strong earthquakes. Since the development of SCFs in 2001, theoretical analysis, experimental testing and numerical modelling of SCFs have been extensively studied by many researchers. Ricles et al. and Garlock et al. [1–4] conducted early experimental studies on self-centering beam-column connections with angles, developing a theoretical moment-rotation curve. Self-centering beam-column connections with T-stub devices was further researched by Aliabadi et al. [5]. And Wang et al. [6] achieved the self-centering function of SCFs by adopting shape memory alloys. Additionally, friction dampers have been introduced to self-centering connections. Various details and friction materials, including nonasbestos organic friction pads, hard steel against brass sheets, mild steel against brass sheets etc., were studied and improved continually to attain more stable energy dissipating capacity [7–13]. Moreover, Belleville Springs used in friction sliding structural connections were researched to deal with the clamping force loss in seismic friction sliders [14]. The proposed self-centering connections or SCFs achieved the resilient function of the structure upon earthquake actions. While the self-centering connections proposed above required on-

site aerial tension of steel strands when they are applied to multi-rise or high-rise buildings, causing great construction difficulty inevitably. Besides, studies about the restraint of the floor system on the self-centering function of SCFs were also conducted by researchers. Garlock et al. [15,16] suggested a type of collector beams to transfer the inertial forces to the frame and to accommodate the expansion effect. Chou et al. [17,18] proposed a composite concrete slab with discontinuity at the column centerline. Kim et al. [19] introduced a detailing between concrete slab and post-tensioned self-centering frame. And Huang et al. [20] proposed an innovative self-centering (SC) coupled-beam system with friction dampers.

Based on the above-mentioned researches, the authors [21] proposed a prefabricated self-centering steel frame (hereafter known as PSCF) containing web friction devices (WFDs), for which the self-centering beams were posttensioned on the ground and then connected with the frame columns in the same way as conventional steel beams did. It could greatly improve the construction efficiency when PSCF was utilized in multi-rise and high-rise buildings. Brass sheets were adopted in WFDs to provide a stable energy dissipation capacity and sufficient durability. Quasi-static tests of eight prefabricated self-centering connections (hereafter known as PSC connections) were conducted and the time-history analysis on the overall structure of PSCF was carried out

---
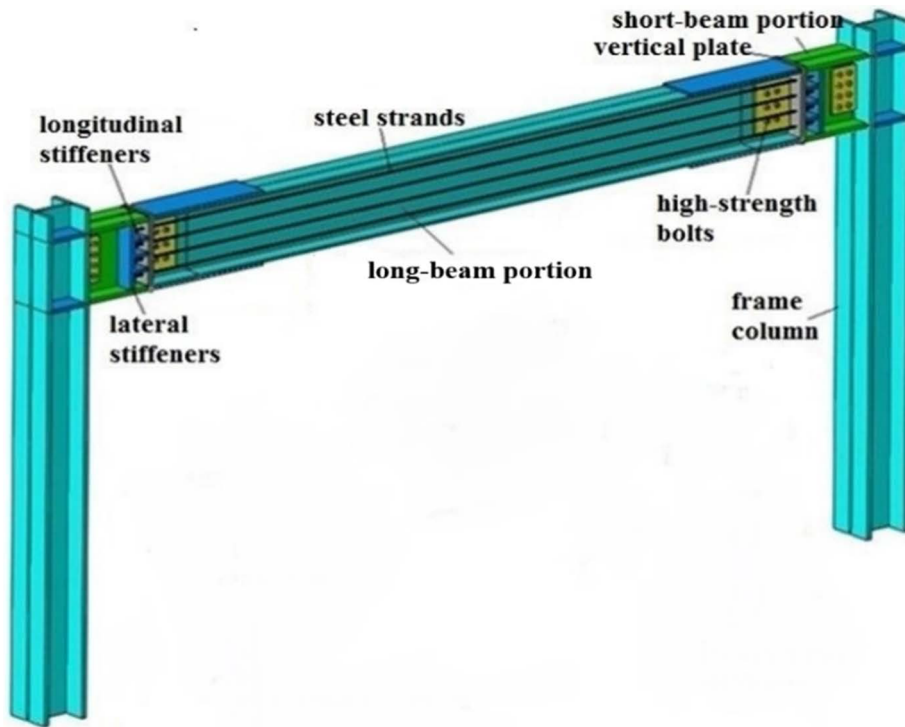
Fig. 1. Details of PSCF.

[22,23,24]. Moreover, pseudo-dynamic experimental researches toward PSCF were also conducted [25] to study its seismic behavior under earthquakes with various magnitudes.

In this paper, a spatial PSCF with a new type of floor system containing sliding secondary beams was proposed based on the completed researches [21–25]. It not only possesses the advantages of PSCFs but accommodates the expansion of frame. Pseudo-dynamic test and quasi-static test were conducted on a 2-story, 2-bay spatial test substructure, to explore and verify the seismic performance of the spatial PSCF and the working mechanism of the new floor system containing sliding secondary beams.

2. Details of the PSCF

The details of the PSCF are illustrated in Fig. 1. Composed of two short-beam portions and a long-beam portion as shown in Fig. 2, the frame beam is assembled by vertical plate, post-tensioned steel strands

Fig. 2. Assembly of frame beam.

and web friction devices (WFDs) at both ends, to mitigate the seismic actions. This innovative type of assembly enables the beams to connect with column as a common type (i.e. mixed welded and bolted beam-column connection) during the construction and avoids the on-site aerial tension work and perforations at column flanges for the anchorage of steel strands, improve the construction efficiency greatly when it is adopted in multi-rise and high-rise buildings.

WFDs are installed at splicing position of long beam portion and short ones symmetrically. Details are illustrated in Fig. 3, where WFD is assembled by the web of long beam portion with slotted holes, shear plates, two pieces of brass sheets sandwiched between the web of long beam portions and shear plates as well as high strength bolts. Here, brass sheets are adopted to achieve a reliable friction behavior and stable energy dissipating capacity, and material property has been validated through the completed test [31].

3. Performance-based design of PSCF

The spatial PSCF was designed to satisfy the following targets [30]: no opening and no damage can be observed when PSCF is subjected to frequent earthquakes; gap openings can be formed to dissipate energy and no damage shall occur in the main components under fortification earthquakes; there is only slight structural damage, the structure still remains serviceable and are able to resist intensive aftershocks upon rare and extremely rare earthquakes. To achieve the design targets above, a detailed design procedure on the PSCF was proposed and illustrated as follows.

3.1. Estimation of the imminent gap-opening moment by structural response

The imminent gap-opening moment of the beam-column connection shall not be less than the maximum flexural moment, to satisfy the "Strong Connection and Weak Component" criterion regulated in Chinese code [26]. In this paper, the imminent gap-opening moment M_{IGO} should satisfy the following requirement.

$$M_{IGO}/M_{des} = 1.1 \sim 1.2 \tag{1}$$
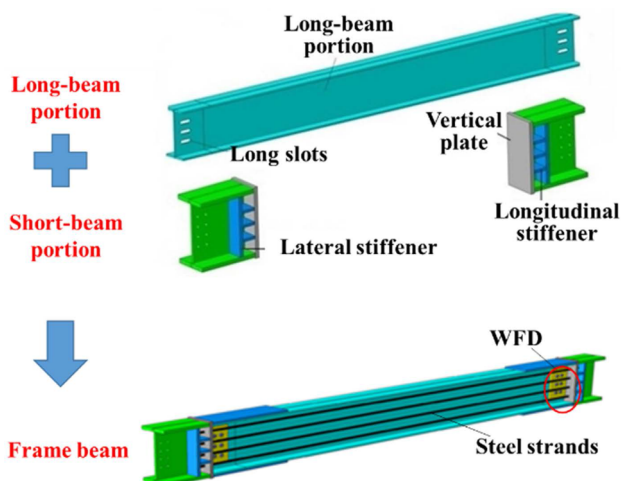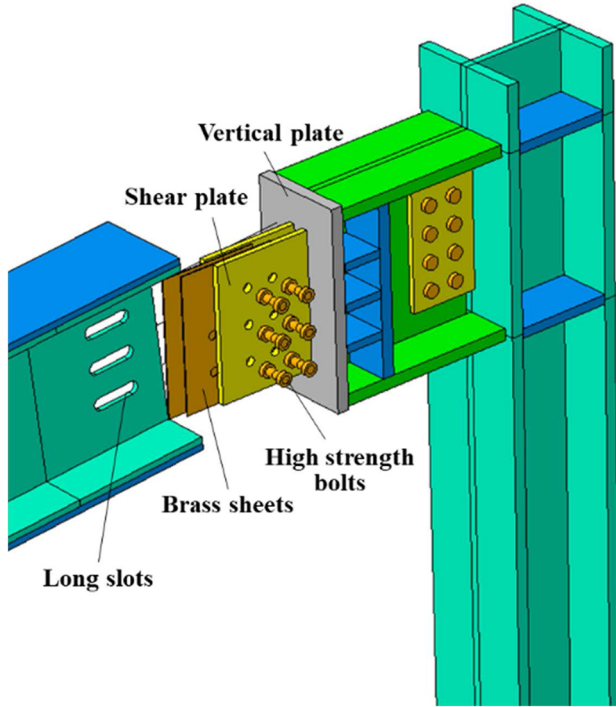
Fig. 3. Illustration of WFDs.

Where M_{IGO} is the imminent gap-opening moment of PSC connections and M_{des} is the maximum flexural moment of PSC connections under frequent earthquakes.

3.2. Design of the decompression moment M_d and the friction moment M_f

The decompression moment (M_d) shall be larger than the friction moment caused by WFDs (M_f), to enable an adequate self-centering capacity of the beam-column connection upon the generation of gap-openings, which implies M_d should not be less than the half of M_{IGO} as shown in Inequality (2). Then, M_f can be obtained by Eq. (3).

$$M_d > 0.5M_{IGO} \tag{2}$$

$$M_{IGO} = M_f + M_d \tag{3}$$

3.3. Design of short beam portion

The criterion of "Strong Column and Weak Beam" should be satisfied during design of short beam portion. Then, the dimensions of the short beam portion shall meet the following requirements as shown in Eqs. (4) and (5).

$$t_{f,S} \geq t_{f,L} + t_{r,L} \tag{4}$$

$$t_{w,S} \geq t_{w,L} \tag{5}$$

Where $t_{f,S}$, $t_{w,S}$ is the thickness of the flange and the web of the short beam portion, respectively; $t_{f,L}$, $t_{w,L}$ refers to the thickness of the flange and the web of the long beam portion, respectively; $t_{r,L}$ is the thickness of the reinforcing plate.

To provide a sufficient stiffness, the length of the short beam portion should be as short as possible under the premise of being available for installation of high-strength bolts and anchorage work of PT strands.

3.4. Design of PT strand

The initial PT force F_0 is determined by Eqs. (2), (3) and (6). To ensure an elastic state of single steel strand, the requirement described in Eq. (7) should also be satisfied. The schematic of the PSC connection at gap opening is shown in Fig. 4.

$$M_f = F_f r, \quad M_d = \sum_{i=1}^{n} F_0 h_i \tag{6}$$

$$F = F_0 + 2\frac{k_b k_s}{k_b + k_s} d_2 \theta_r \leq F_y \tag{7}$$

$$\theta_{r,max} = \frac{(F_y - F_0)}{2d_2} \frac{(k_b + k_s)}{k_b k_s} \tag{8}$$

Where F_y is the yield force of single steel strand; h_i is the distance from the strand i to the rotation center; r is the distance between the center of rotation and the centroid of the friction force; F_f is the friction force caused by WFDs as shown in Fig. 4; k_b is the axial linear stiffness of the beam section, and the calculated length is the span of PSCF; k_s is the linear axial stiffness of the steel strands, the effective length is the span
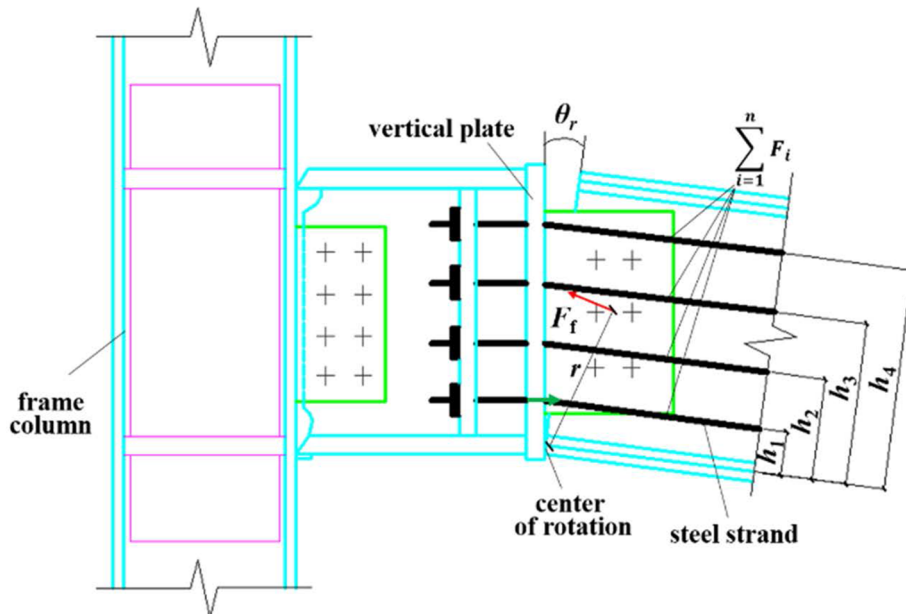
Fig. 4. Schematic of gap opening of the PSC connection.

(a) Illustration under no lateral force condition (b) Illustration under maximum gap-opening condition
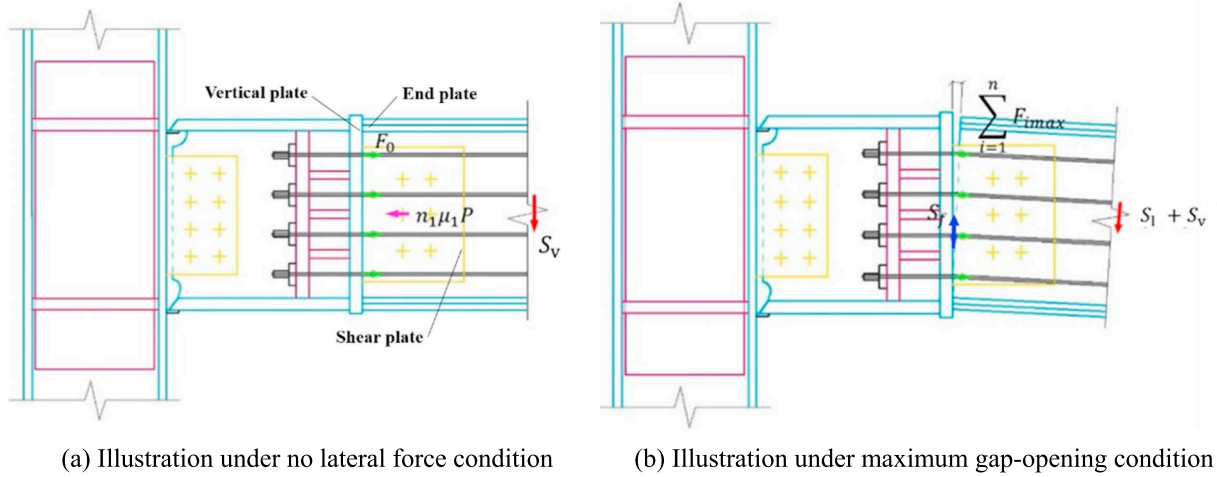
Fig. 5. Schematic of anti-shear calculation for the PSC connection. (a) Illustration under no lateral force condition. (b) Illustration under maximum gap-opening condition.

of PSCF and the calculating area is the sum of all strands; θ_r is the relative rotation of the PSC connection; $\theta_{r,max}$ is the maximum relative rotation of the PSC connection.

3.5. Shear check of the PSC connection

Due to the existed shear force imposed on the PSC connection, two loading conditions have been considered to check the shear resistance of the connection. Firstly, when the lateral force is not applied on the connection as shown in Fig. 5(a), the maximum static friction force between the end plate of long beam portion and the vertical plate ($S_{sf,max}$) should be larger than the vertical shear force. Meanwhile, the compression force between the end plate and the vertical plate (F_c) as given in Eq. (9), may be reduced by the horizontal friction load between the shear plate and the long beam webs (i.e. $n_1\mu_1 P$, as shown in Fig. 5(a)). The following Eq. (10) should be satisfied.

$$F_c = F_0 - n_1\mu_1 P \tag{9}$$

$$S_{sf,max} = \mu F_c > S_v \tag{10}$$

Where F_c is the compression force between the end plate and the vertical plate; F_0 denotes the initial PT force; P is the pretension of the bolt, which is determined according to Chinese code [29]; n_1 is the number of friction surfaces; μ is the friction coefficient between the long beam and the vertical plate, for which the value is 0.48 according to the conducted friction test [31]; μ_1 is the friction coefficient between the brass sheet and the web of the beam, which is 0.34 according to the completed friction test [31]; S_v is the shear caused by the vertical load. $S_{sf,max}$ denotes the maximum static friction force between the end plate of long beam portion and the vertical plate.

Secondly, when gap-opening reaches the maximum value as shown in Fig. 5(b), the PSC connection was subjected to the dual effects of vertical shear (S_v) and lateral load (S_l). While the shear resistance is composed of two portions, i.e. the friction force between the end plate the long beam and the vertical plate ($S_{f,max}$) and the shearing capacity of the welds between the shear plate and the vertical plate (S_s). Therefore, the following Inequality (12) shall be met.

$$S_{f,max} = \mu \sum_{i=1}^{n} F_{i\,max} \tag{11}$$

$$S_{f,max} + S_s > S_l + S_v \tag{12}$$

Where $S_{f,max}$ denotes the maximum friction force between the end plate of the long beam and the vertical plate; $F_{i max}$ represents the maximum PT force of the i_{th} strand; S_s is the shearing capacity of the welds

between the shear plate and the vertical plate; and S_l is the shear force caused by the lateral force.

3.6. Design of the slotted hole of the web

The slotted hole on the web is designed on the basis of maximum gap–opening and the sizes should be determined according to Eqs. (13) and (14).

$$W_{eh} = 2D_{x1}\theta_{r,RE} + d + 4mm \tag{13}$$

$$L_{eh} = D_{x2}\theta_{r,RE} + (D_{x1} - D_{x2})(d + 4mm) \tag{14}$$

Where, W_{eh}, L_{eh} denotes the with and length of the slotted hole, respectively; D_{x1} is the distance from the furthest friction bolt to the center of rotation; $\theta_{r,RE}$ is the connection gap-opening rotation under the action of rare earthquakes; and d is the diameter of high strength bolts; D_{x2} represents the distance from the nearest friction bolt to the center of rotation.

3.7. Design of the reinforcing plate on flange of the PSC beam

When gap-opening occurs at the PSC connection, both the beam flange and the reinforcing plate are compressed, and there is no contact between the beam web and the vertical plate. Therefore, the length that the web is subjected to the shear load, is equal to the length of the reinforcing plate at the flange. If the column deformation was ignored, the expansion effect of the PSCF would exert due to the generation of the PSC connection gap-opening. It can be simplified that the shear force of the web is equal to the yielding load of the steel strands, as shown in Eq. (15):

$$L_{rp}\tau_{w,y}t_w = n_s F_{y1} \tag{15}$$

Where L_{rp} is the length of reinforcing plate of the beam flange; $\tau_{w,y}$ is the yield shear stress of the beam web; t_w is the thickness of beam web; F_{y1} is the yield force of single steel strand; and n_s is the number of steel strands.

4. General conditions of testing model

4.1. Prototype structure

The prototype structure was designed with a servicing life of 50 years, for which the structural safety grade is the second grade [32], the seismic fortification is class B, the site classification is type III, the seismic fortification intensity is 8 degree and the design basic
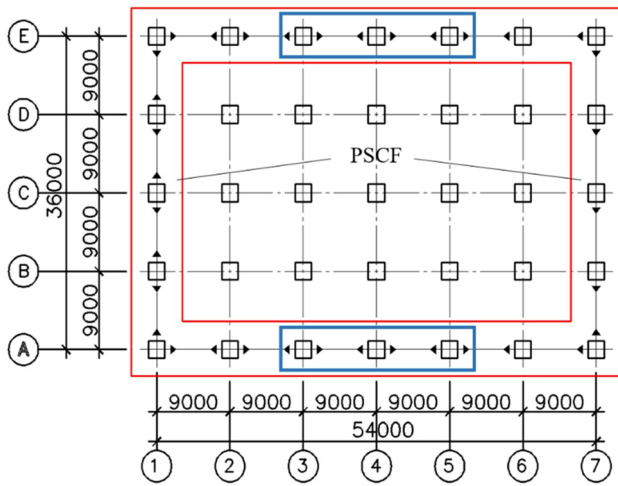
Fig. 6. Plan of prototype structure.
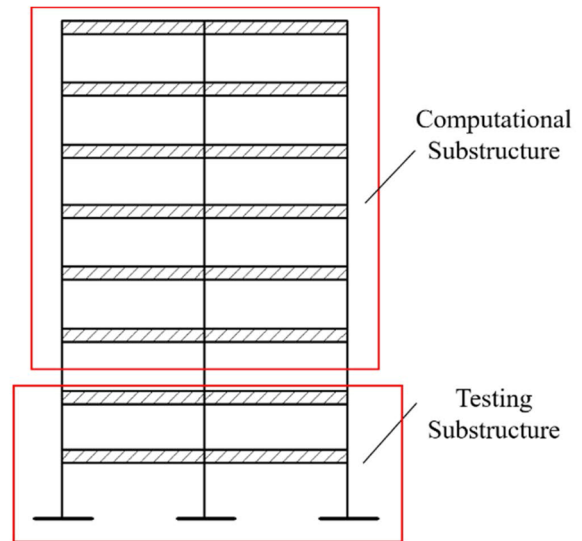
Fig. 7. Schematic of testing model.

acceleration of ground motion is 0.2 g in accordance with Chinese *Code for Seismic Design of Buildings* [26]. The floor dead load, which includes the weight of the floor diaphragm, is 7.0 kN/m²; the floor live load is 2.0 kN/m²; and the roof live load is 2.0 kN/m².

Based on the design criteria described previously, the prototype structure is designed and the plan view is illustrated in Fig. 6. It has 8 stories, 4 spans in transverse direction and 6 spans in longitudinal direction, where each span is 9 m for both directions. The height for the first floor is 4.2 m, and is 3.3 m for floors 2–8. The steel frames bracketed by the red box refers to PSCF, where the frame columns adopt box section (□400 mm × 400 mm × 34 mm), and the frame beams are H-shaped section (H750mm × 350 mm × 22 mm × 28 mm). The rest area is designed as the gravity system, for which the column sections are in box shape (□500 mm × 500 mm × 24 mm) and the beams adopt H-shaped section (H750mm × 350 mm × 22 mm × 28 mm). The PT strand is 1 × 19 type with a nominal diameter of 21.8 mm and a tensile strength (T_u) of 1860 MPa.

4.2. Testing model

The testing model is selected by the blue box as shown in Fig. 6. Pseudo-dynamic test has been conducted on 8-story, 2-bay testing model that consists of a 2-story, 2-bay testing substructure and a 6-story, 2-bay computational substructure as shown in Fig. 7. The plan of the testing substructure with WFDs is shown in Fig. 8.

Considering the conditions of laboratory, the testing model is scaled down to 0.3 times of the prototype structure. All dimensions are adjusted according to the Similarity Theory and the similarity relation of the model is illustrated in Table 1.

Therefore, the height of the first floor is 1.26 m and is 1.0 m for floors 2–8. The dimension of the frame column, the long-beam portion and the short-beam portion is H200mm × 200 mm × 10 mm × 14 mm, H194mm × 150 mm × 6 mm × 9 mm, and H204mm × 150 mm × 8 mm × 14 mm, respectively. The reinforcing plate is 6 mm in thickness and 300 mm in length. Besides, the axial compression ratio of the frame columns in substructures is consistent with that of prototype structure. The geometrical and physical properties of the steel strands are same as that of the prototype structure. Moreover, the ratio of the decompression moment M_{IGO} to the maximum flexural moment at the beam-column connection M_{des} remains a constant before and after scaling. M20 high-strength bolts of grade 10.9 specified in Chinese code [29], are adopted in the PSC connections and common beam-column connections. Here, "grade 10.9" means the ultimate tensile strength and the yield ratio of the high-strength bolt is 1000Mpa and 0.9, respectively; "M20" means the nominal diameter of the high-strength bolt is 20 mm.

4.3. New floor system

When the common floor system is used in the PSCF, the gap opening mechanism of beam-column connection may be restricted. The floor system proposed by the authors is designed with a new type of secondary beams. Fig. 9 illustrates the details of the new-type secondary beams, which are able to slip under the action of lateral forces. Slotted holes are located at each end of the web of secondary beams, and Teflon plates are sandwiched between the web of the secondary beam and the
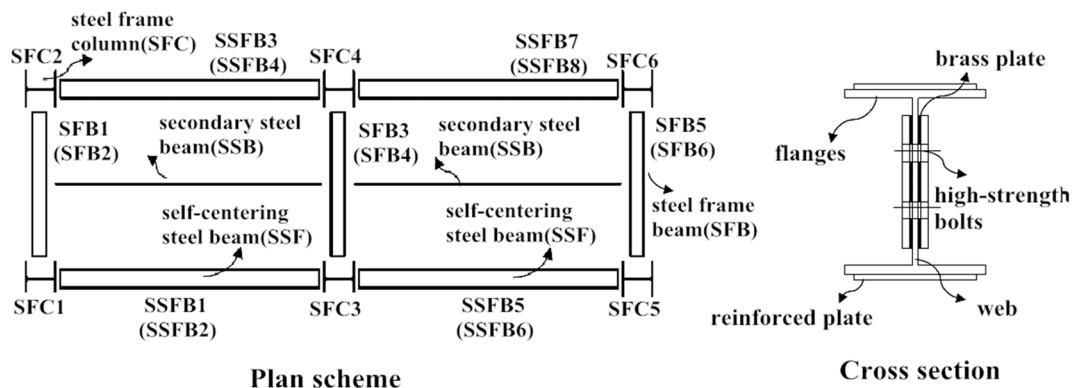
Fig. 8. Plan of the testing substructure.

Table 1
Similarity relation of the model.

	Length	Stress	Axial compression ratio	Time
Similarity coefficients	0.3	1	1	$(0.3)^{0.5}$
Dimensions	L	FL^{-2}	1	T

connecting plate with a friction coefficient of 0.04 against the steel. It can effectively decrease the friction force between contact surfaces, reduce or even eliminate the restraints to the deformation of PSCF. Non-continuous, non-composite slabs with profiled steel sheets are used in the testing substructure, which not only enables the working mechanism but ensures the overall stability of secondary beams.

4.4. Material properties

The steel utilized in the testing substructure is Q345B, and there are five types of steel plates with thicknesses varying from 6 mm to 14 mm. Material properties of steel plates are presented in Table 2. Mechanical properties of steel plates adopted in the calculation of the testing model are based on the average values obtained from the tests. The material properties of steel strands are given in Table 3.

4.5. Establishment of PT force and preload

The initial PT force (F_0) was accurately achieved and controlled by a set of tensioning technology. As shown in Fig. 10, a hydraulic jack was used to conduct the tensioning operation and meanwhile, the real-time PT force was collected by a pressure sensor and displayed on the monitor screen. By adjusting the precession of the anchor nut as shown in Fig. 10(d) and over tensioning the steel strand, the initial PT force F_0 can be reached accurately.

The installation of high-strength bolts could be divided into two stages: initial screwing and final screwing. In the initial screwing stage, the bolts were tightened manually; in the final screwing stage, the expected preload of bolts were achieved by an electric torque wrench for special use as shown in Fig. 11. The relevant operations were regulated in *Technical Specifications for high strength bolt connections of steel structures* [29].

5. Pseudo-dynamic test

5.1. Loading regime and input parameters

The schematic of the working process of pseudo-dynamic test is shown in Fig. 12. Considering the self-centering characteristic of the
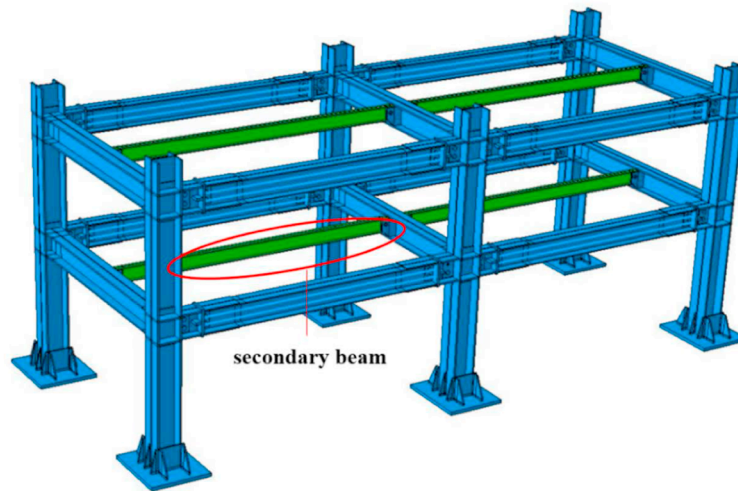
(a) Schematic of secondary beams
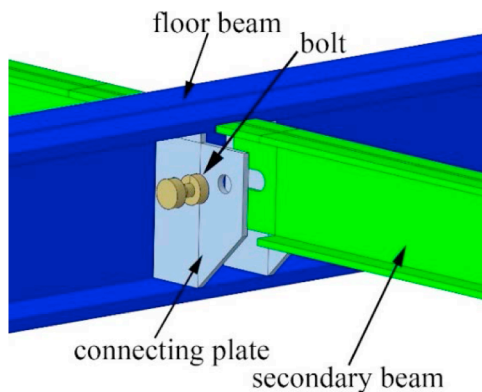
(b) Details of secondary beams (disassemble)
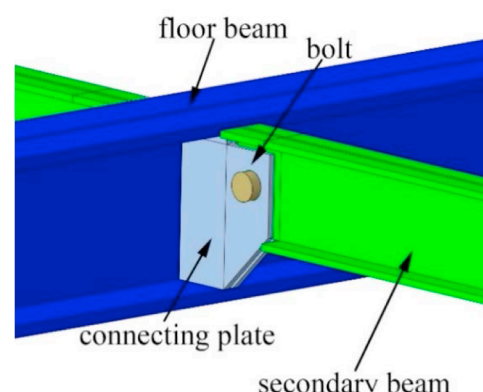
(c) Details of secondary beams (assemble)

Fig. 9. Details and schematic of slipping secondary beam. (a) Schematic of secondary beams. (b) Details of secondary beams (disassemble). (c) Details of secondary beams (assemble).

Table 2
Material properties for standard steel plates.

Thickness (mm)	Elasticity modular (10^3 N/mm^2)	Yield strength (N/mm^2)	Tensile strength (N/mm^2)	Elongation rate
6	205.5	381.5	481.8	24.6%
8	209.3	408.8	548.5	24.5%
10	205.7	432.8	559.0	25.8%
12	206.0	451.4	574.5	27.4%
14	208.6	377.3	494.9	29.0%

Table 3
Material properties for steel strands.

Strand	Specimen	Yield strength (MPa)	Ultimate strength (MPa)	Elastic modulus (GPa)
1 × 19	1	1728.3	1894.5	2.03
1860 MPa	2	1727.1	1895.8	2.05
	3	1732.8	1875.4	2.00
	Average value	1729	1899	2.03

PSCF, the multi-story structural remote cooperative pseudo-dynamic test platform (NetSLab_MSBSM1.0.0) developed by Prof. Guo et al. [27] was utilized, to control the loading process and conduct the numerical calculation. The double-flag shaped hysteretic models of each floor and the seismic ground motions should be input into the platform before loading. MTS hydraulic servo testing system was adopted to carry out the displacement loading on testing substructure, collect the feedback force and deliver the data to the controller and computation device of the platform. According to the feedback force, the dynamic equation of the structure is solved iteratively in computation platform as shown in Eq. (16), determining the computational displacement of the next loading step. Then the controller would command the loading system to continue the displacement loading. By repeating the steps above until

Fig. 11. Final screwing of high-strength bolts.

the whole seismic ground motion record was input into the loading system, the pseudo-dynamic test of the testing substructure was successfully achieved.

$$[M]\ddot{u} + [C]\dot{u} + [P] = [M]\ddot{u}_g \tag{16}$$

Where $\ddot{u}$, $\dot{u}$, $[P]$ refers to the vectors of acceleration, velocity and restoring force, respectively; $[M]$, $[C]$ is the mass and damping matrix, respectively; $\ddot{u}_g$ is the input acceleration vector of seismic ground motion.

During the loading process of pseudo-dynamic test, a series of parameters were required to input into the computational platform, including the structural stiffness before and after gap opening occurrence (denoted as K_1 and K_2) and the story displacement corresponding with the critical moment and the maximum gap-opening (denoted as d_1 and d_2). Here, the restoring force hysteretic model in double-flag shape was input into the platform according to the shear-displacement relation as the story drift reached the elastoplastic limit (i.e. 0.02 rad). For the testing substructure, the mass of each floor and the theoretical inter-story restoring force are necessary to be input into the pseudo-dynamic

(a) Hydraulic jet

(b) Pressure sensor

(c) Pressure monitor

(d) Ajdustment of PT force
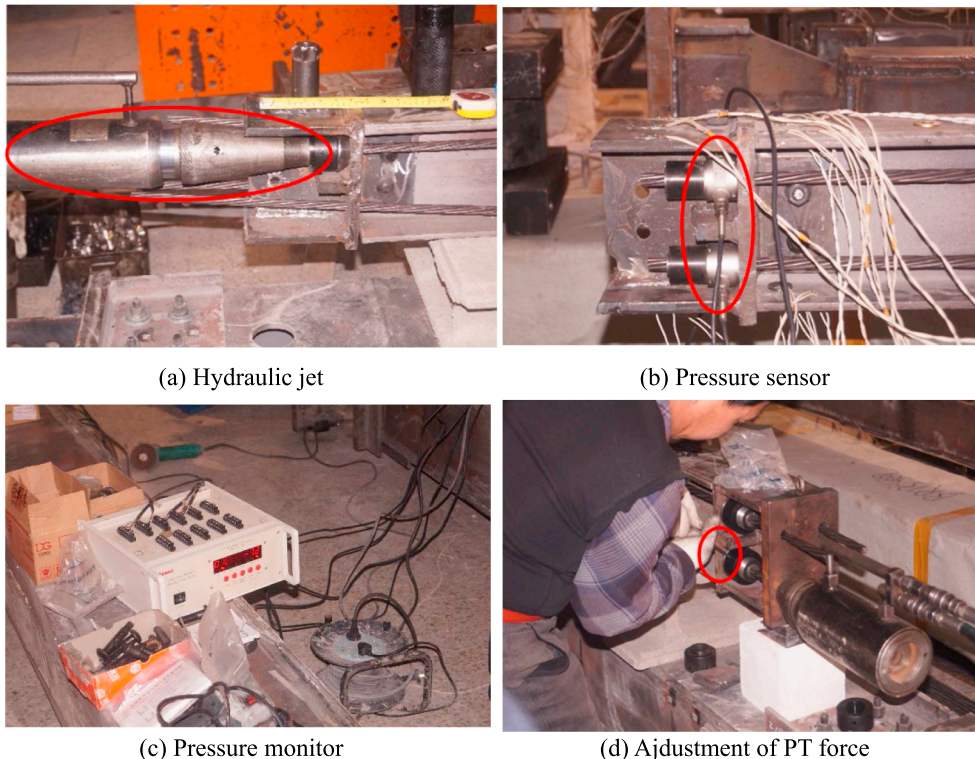
Fig. 10. Determination of PT force. (a) Hydraulic jet. (b) Pressure sensor. (c) Pressure monitor. (d) Ajdustment of PT force.
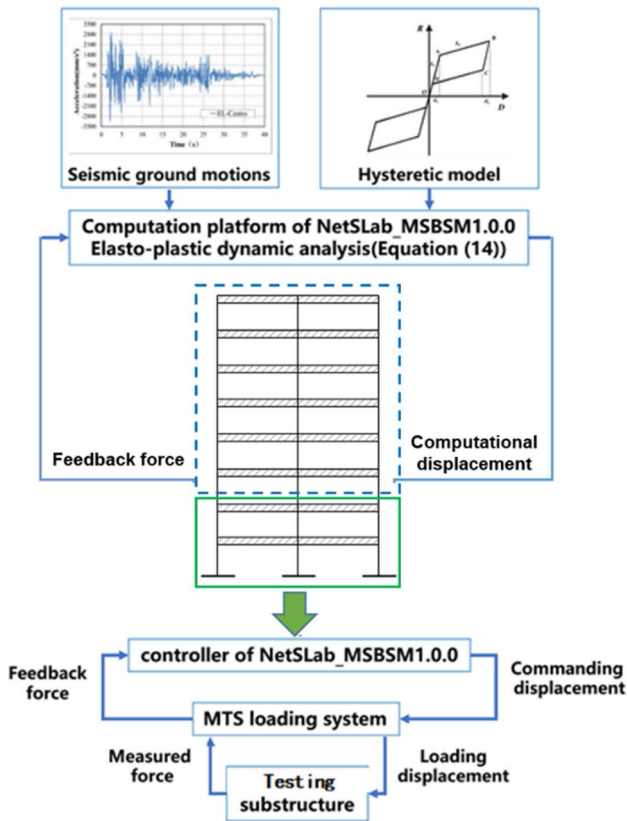
Fig. 12. Schematic of loading process of pseudo-dynamic test.

Fig. 13. Illustration of loading equipment.

Fig. 14. EL-Centro ground motion record.
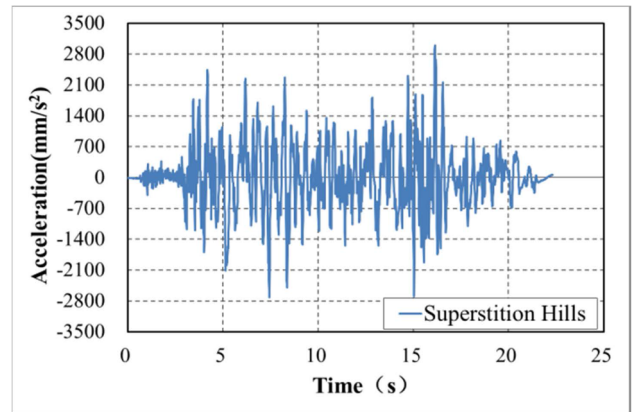
Fig. 15. Superstition Hills ground motion record.
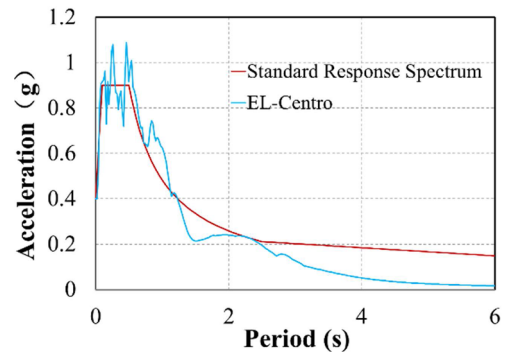
Fig. 16. EL-Centro Acceleration response spectrum.
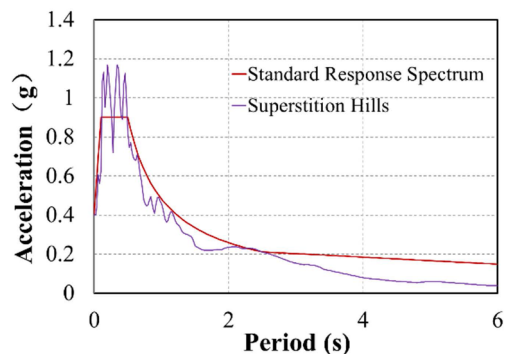
Fig. 17. Superstition Hills Acceleration response spectrum.

test platform. During the pseudo-dynamic test as illustrated in Fig. 13, the displacement loading are applied through two 200 t actuators. In order to have a similar axial compression ratio with the prototype structure, vertical loads are applied to the top of columns through reaction frame, 100 t and 200 t actuators, and loading beams.

5.2. Seismic ground motions

El-Centro (EL) and Superstition Hills (SH) seismic ground motions were selected to conduct the pseudo-dynamic tests and the acceleration time-history curves are shown in Fig. 14 and Fig. 15, for which the time step is 0.1 s. According to the Similarity Theory, the time step was adjusted to 0.0086 s. The peak ground acceleration (thereafter known as PGA) of both seismic ground motions was adjusted to 0.4 g. In addition, the time history curves were converted to acceleration response spectra using the SeismoSignal software as shown in Figs. 16 and 17.

Fig. 18. Arrangement of displacement meter and bolt pressure sensors.
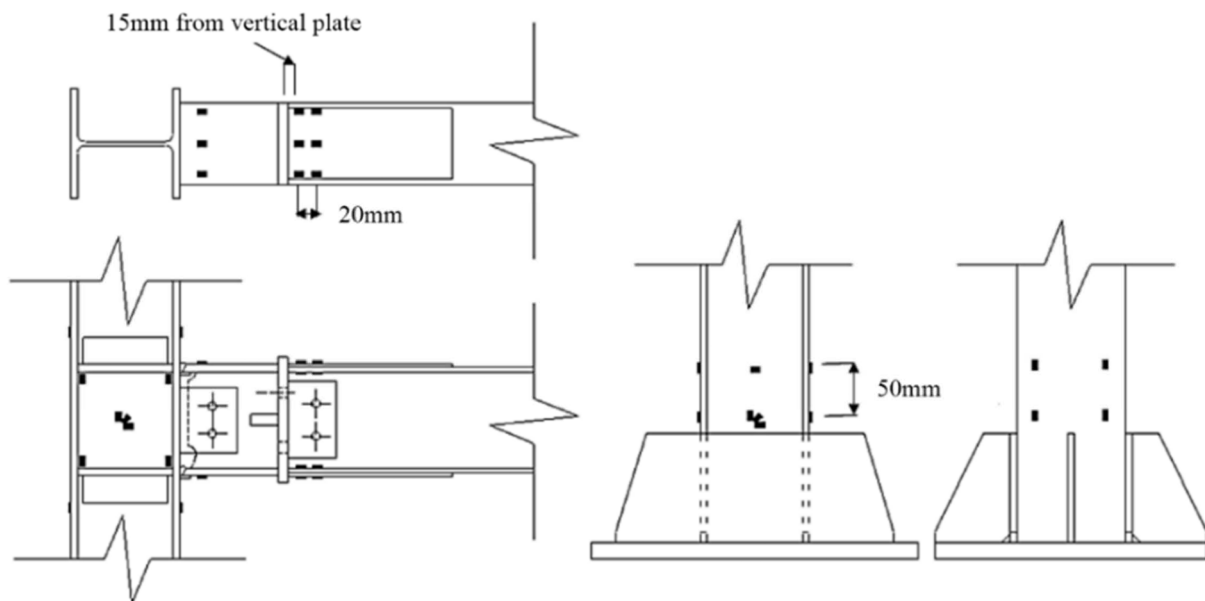
Fig. 19. Arrangement of strain gauges.

The first period and the damp coefficient of the testing model was 1.1247 s and 0.05, respectively. Both response spectrum curves essentially coincided with the standard response spectrum curve [26] at the first period. Peak values of the seismic acceleration records are adjusted to 0.07 g, 0.2 g, 0.4 g, 0.51 g, 0.62 g, 0.8 g and 1.0 g, where the first 5 magnitudes correspond to the 8-degree frequent, fortification, rare, 8-degree rare (0.3 g), and 9-degree rare earthquakes specified in *Chinese Code for Seismic Design of Buildings* [26]. The recurrence probability of frequent, fortification and rare earthquake in 50 years, reaches 63.2%, 10% and 2%, respectively.

5.3. Instrumentation

The arrangement of displacement meters is shown in Fig. 18. Load cells are contained in both vertical and lateral actuators to collect the data of axial and the reaction forces of the testing substructure. A 30 t pressure sensor is implemented in each strand to monitor the variation

of cable force; 6 bolt pressure sensors are applied in critical junctions of the spatial structure to collect the forces of the bolts, as shown in the red dashed boxes in Fig. 18. Eight displacement meters are arranged at the external surface of column flange to measure the story displacements; linear displacement potentiometers are fixed on the junctions of the self-centering connections to measure the gap openings; the displacement meters are fixed at the ends of secondary beams to monitor the slippage of secondary beams. Additionally, strain gauges are placed to measure the strains in both the flanges and the webs of the column bases, top and bottom beam flanges and the joint region, as shown in Fig. 19. Photos of the measuring instruments are shown in Fig. 20.

6. Results and discussion of Pseudo-dynamic test

6.1. Under the seismic ground motions with PGA = 0.07 g to 0.51 g

Under the action of both seismic ground motions with PGA = 0.07 g
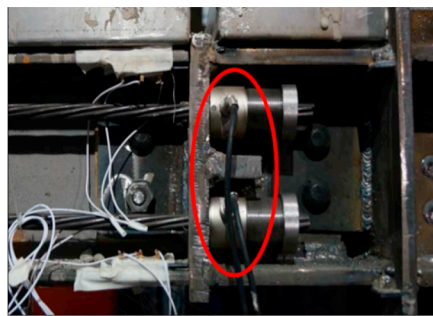
(a) Pressure sensors for steel strands
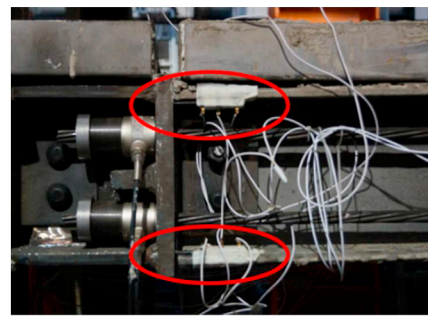
(b) Linear displacement potentiometers

(c) Displacement meter

(d) Pressure sensor for bolts

Fig. 20. Photos of measuring instruments. (a) Pressure sensors for steel strands. (b) Linear displacement potentiometers. (c) Displacement meter. (d) Pressure sensor for bolts.
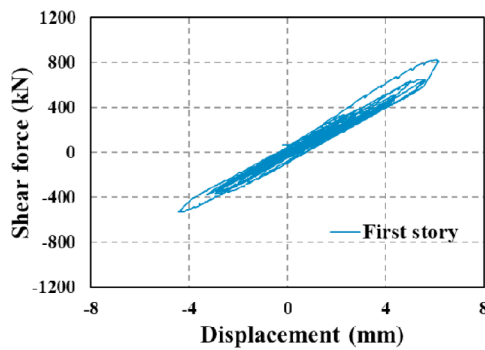
(a) Curves with PGA=0.4g
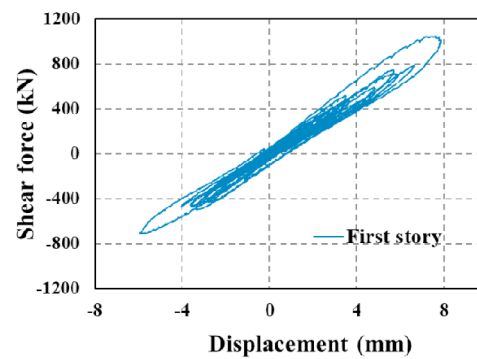
(b) Curves with PGA=0.51g

Fig. 21. Shear force-displacement curves for the first story of the testing substructure under El-Centro seismic ground motion. (a) Curves with PGA = 0.4 g. (b) Curves with PGA = 0.51 g.
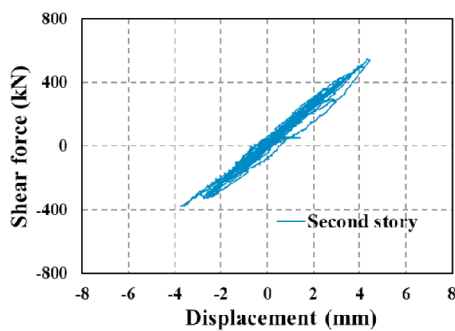
(a) Curves with PGA=0.4g
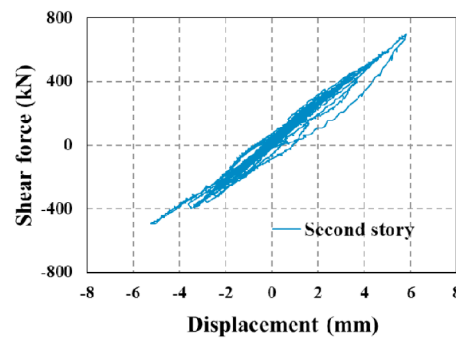
(b) Curves with PGA=0.51g

Fig. 22. Shear force-Displacement curves for the second story of the testing substructure under El-Centro seismic ground motion. (a) Curves with PGA = 0.4 g (b). Curves with PGA = 0.51 g.

(a) PGA=0.07g

(b) PGA=0.2g
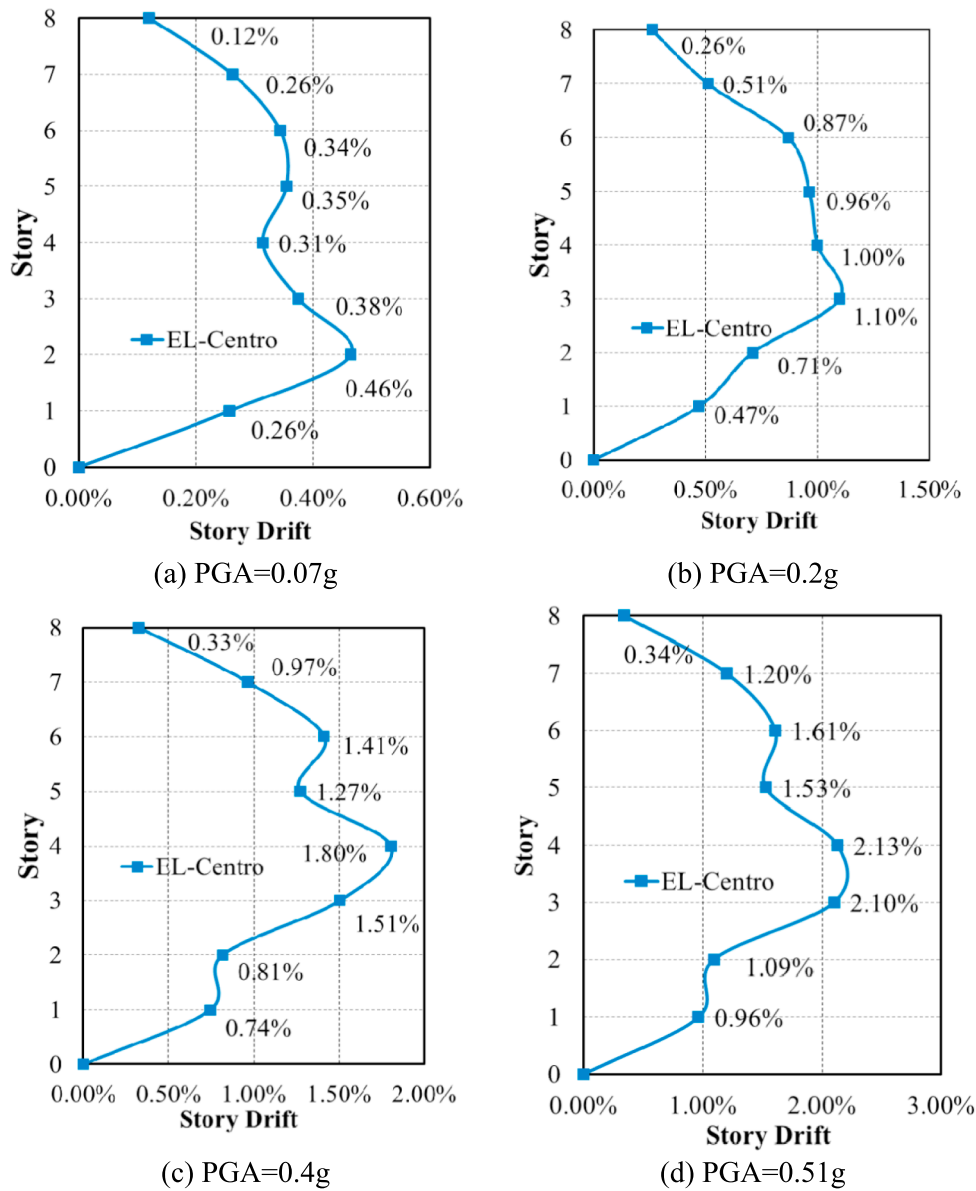
(c) PGA=0.4g

(d) PGA=0.51g

Fig. 23. Story drift of the testing model. (a) PGA = 0.07 g. (b) PGA = 0.2 g. (c) PGA = 0.4 g. (d) PGA = 0.51 g.

(a) PGA=0.62g
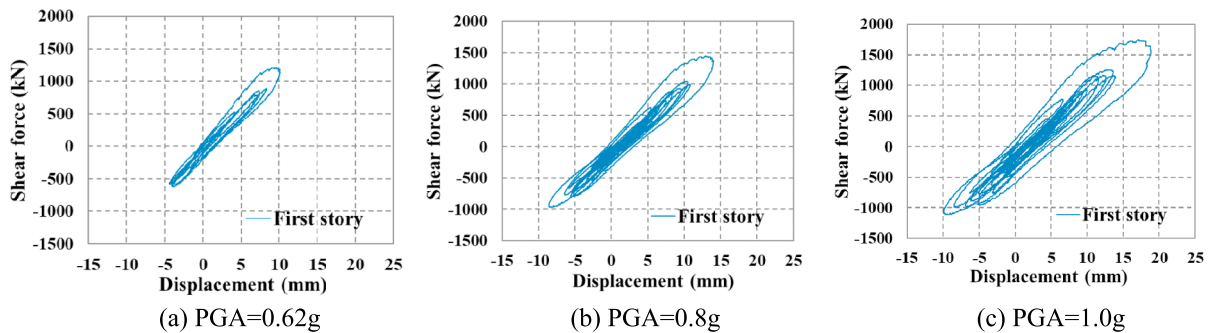
(b) PGA=0.8g

(c) PGA=1.0g

Fig. 24. Hysteretic curves for the first story of the testing substructure. (a) PGA = 0.62 g. (b) PGA = 0.8 g. (c) PGA = 1.0 g.

to 0.51 g, the structural responses are still at a relatively low level. And the whole testing substructure remains in the elastic state, with the maximum story displacement response taking place in the computational substructure.

6.1.1. Hysteretic curves

The base shear-displacement curves of the first story and the second story of the testing substructure under the action of El-Centro seismic record with PGA = 0.40 g and 0.51 g are presented in Fig. 21 and Fig. 22, respectively. When PGA is 0.4 g, the story drifts of the first and the second story are 0.5%rad and 0.53%rad, respectively, with the

(a) PGA=0.62g   (b) PGA=0.8g   (c) PGA=1.0g
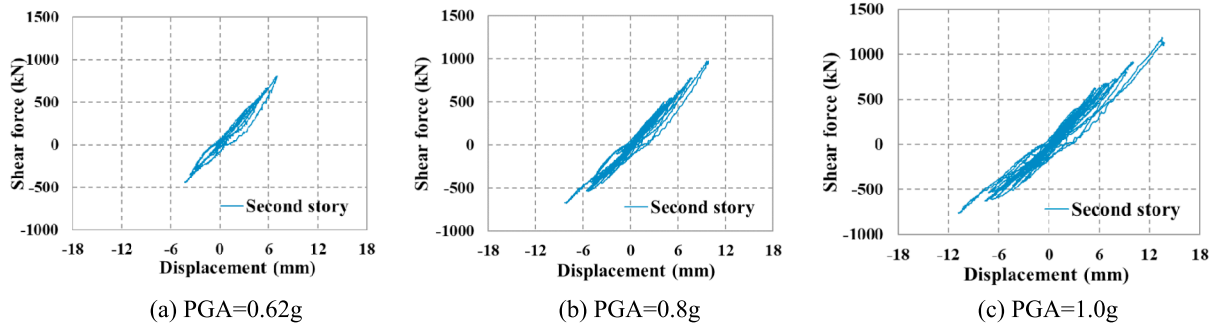
Fig. 25. Hysteretic curves for the second story of the testing substructure. (a) PGA = 0.62 g. (b) PGA = 0.8 g. (c) PGA = 1.0 g.
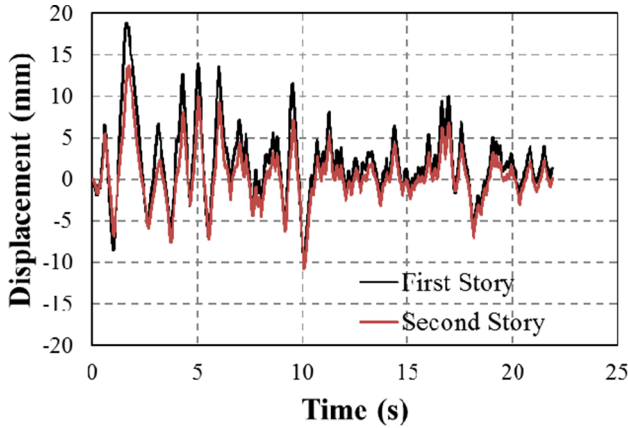
Fig. 26. Time-history curve of the displacement when PGA = 1.0 g.

Table 4
Story drift and gap opening of the structure.

Seismic ground motion	Story	PGA	$\theta_{s,max}$ (%rad)	$\theta_{s,res}$ (% rad)	$\theta_{r,max}$ (%rad)		$\theta_{r,res}$ (%rad)	
					East	West	East	West
EL	First story	0.62 g	0.80	0.029	0.52	0.43	0.015	0.010
		0.8 g	1.11	0.061	0.75	0.65	0.005	0.005
		1.0 g	1.50	0.106	1.21	0.90	0.052	0.010
	Second story	0.62 g	0.56	0.048	0.31	0.24	0.000	0.041
		0.8 g	0.98	0.003	0.49	0.38	0.005	0.005
		1.0 g	1.09	0.017	0.77	0.68	0.000	0.010
SH	First story	0.62 g	0.73	0.017	0.55	0.46	0.015	0.021
		0.8 g	0.97	0.025	0.79	0.64	0.077	0.005
	Second story	0.62 g	0.61	0.017	0.36	0.27	0.005	0.005
		0.8 g	0.97	0.013	0.63	0.54	0.010	0.000

corresponding maximum displacements of 6.31 mm and 5.30 mm, respectively. Under the seismic action with PGA = 0.51 g, the maximum story drifts at the same positions increase to 0.63%rad and 0.65%rad, respectively, with the corresponding maximum displacements reaching 7.88 mm and 6.48 mm, respectively. It is indicated that the displacement responses remain at a relatively low stage at this moment. And the hysteretic curves can be regarded as a linear shape without considering the gaps between the loading devices and the testing substructure.

6.1.2. Story drift
Fig. 23 illustrates the maximum story drifts of the testing model. Under the seismic action with PGA = 0.07 g, the maximum story drift generated in the second story of the testing model reaches 0.46%rad, which has exceeded the elastic story drift limit (i.e. 0.4%rad) specified in standards [26]. When the magnitude increases to 0.4 g, the maximum story drift generated in the fourth story of the testing model is 1.79%rad, not exceeding the elastic-plastic story drift limit (2%rad)

specified in standards [26]. Under the seismic action with PGA = 0.51 g, the maximum story drift reaches 2.13%rad, occurring at the fourth story of the testing model. From the story drift curves under various magnitudes illustrated in Fig. 23, it can be seen that the variation trend of the story drift curves for the testing model are similar to each other under various earthquake magnitudes, and no mutation phenomenon is observed from the story drift curve.

6.2. Under seismic ground motions of PGA = 0.62 g to 1.0 g

To investigate the seismic performance of the testing substructure under larger magnitudes, experimental research was carried out under seismic ground motions with PGA varying from 0.62 g to 1.0 g.

6.2.1. Hysteretic behavior
The base shear-displacement curves of both stories of the testing substructure under El-Centro seismic record with PGA = 0.62 g to 1.0 g are presented in Fig. 24 and Fig. 25. It can be indicated from the figure that the energy dissipation kept growing with the increase of the seismic magnitude. Under the seismic ground motion with PGA = 0.62 g, 0.8 g and 1.0 g, the maximum base shears of the structure reached 1212.39 kN, 1449.83 kN and 1752.61 kN, correspondingly. The maximum story drift of the first story reached 1.5%rad under the magnitude of PGA = 1.0 g. At the initial loading stage, there exists a slight slippage due to the unavoidable gaps between the loading devices and the testing substructure, for which the hysteretic curves show a slight loop. Simultaneously, both the displacement responses and the gap openings remain at a relatively low level under various magnitudes. As a result, the hysteretic curves for the second story basically showed a linear relation and for the first story, it presented a slight spindle shape due to the existed gaps between the loading devices and the testing substructure.

6.2.2. Displacement and gap opening
In order to investigate the displacement responses of the testing substructure, the measured displacement at FC4 was analyzed. Four connections on two sides of FC3 were also selected to monitor the variation of the gap opening. The variation trends of the displacement responses under various earthquake magnitudes are basically consistent. Therefore, the most representative time-history curve regarding the displacement under the action of El-Centro record with PGA = 1.0 g is shown in Fig. 26. It can be seen that the displacement response of the structure is close to zero at the end of loading process, which indicates the structure has restored to its initial position.

Table 4 lists both the displacement and the gap opening of the structure, in which $\theta_{s,max}$ and $\theta_{s,res}$ represent the maximum story drift and the maximum residual story drift, respectively; $\theta_{r,max}$ and $\theta_{r,res}$ denote the maximum gap opening and the maximum residual gap opening, respectively. Taking the testing results under El seismic record as an example. When PGA is 0.62 g, the maximum story drifts are 0.8% rad and 0.56%rad for the first and the second story of the testing
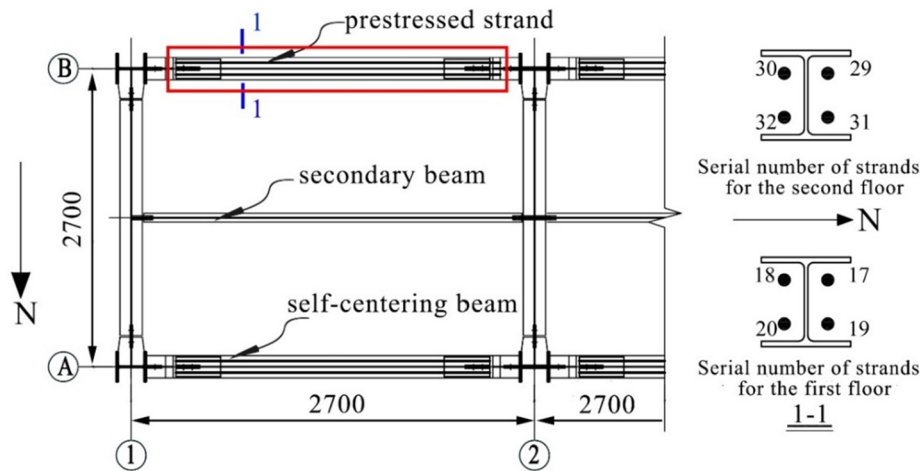
Fig. 27. Position and number of PT strand.

Table 5
PT force variation when PGA = 1.0 g.

Ground motion		Cable 17 (kN) $T_{17}\text{max}/T_u$	Cable 18 (kN) $T_{18}\text{max}/T_u$	Cable 19 (kN) $T_{19}\text{max}/T_u$	Cable 20 (kN) $T_{20}\text{max}/T_u$	Cable 29 (kN) $T_{29}\text{max}/T_u$	Cable 30 (kN) $T_{30}\text{max}/T_u$	Cable 31 (kN) $T_{31}\text{max}/T_u$	Cable 32 (kN) $T_{32}\text{max}/T_u$
EL-Centro	Initial	63.87	65.12	61.84	62.47	64.19	63.74	62.95	61.44
		0.245	0.250	0.237	0.240	0.247	0.245	0.242	0.236
	Maximum	78.68	78.31	75.98	76.74	76.61	77.12	74.50	74.34
		0.302	0.301	0.292	0.295	0.294	0.296	0.286	0.285
	End	63.81	65.24	61.72	62.41	64.31	63.62	63.07	61.62
		0.245	0.251	0.237	0.240	0.247	0.244	0.242	0.237

substructure, with the maximum gap opening reaching 0.52%rad and 0.31%rad, correspondingly. With the increase of seismic intensities, the seismic responses keep growing. When PGA increases to 1.0 g, only the seismic ground motion EL has been applied on the testing substructure to investigate the structural performance. The maximum story drift of the first story is 1.5% rad, approaching the elastic-plastic story drift limit (2%rad) specified in *Code for Seismic Design of Buildings* [26], with the maximum residual story drift valuing 0.106%rad. For the second story, the maximum story drift is 1.09%rad with an even smaller residual story drift valuing 0.017%rad, indicating that the testing substructure has favorable self-centering behavior. The maximum gap opening of the first story reaches 1.21%rad with the maximum residual gap opening of only 0.052%rad, which indicates that the application of the new type secondary beam has enabled the smooth running of the gap opening-closing mechanism of the connection.

6.2.3. Cable force

Eight steel strands of the SCB3 and SCB4 are selected to observe the cable force variation and their positions are shown in Fig. 27.

The initial PT force (F_0) is around 65kN (the error was 1kN), and the ultimate cable force (T_u) is 260.4kN. Therefore, the initial PT force is $0.25T_u$. Under El-centro and Superstition Hills ground motions with PGA = 0.62 g, the maximum cable forces reach 69.25kN ($0.266T_u$) and 69.43kN ($0.267T_u$), respectively. After the loading history with PGA = 0.62 g, the minimum cable force is $0.237T_u$, indicating a 5.2% reduction compared to the initial PT force. The cable force continues to increase with the expansion of gap-opening under larger seismic magnitudes. When PGA reaches 0.8 g, the maximum cable forces under the action of El-centro and Superstition Hills ground motions, increase to 73.5 kN ($0.282T_u$) and 75.47 kN ($0.29T_u$), respectively. The minimum PT force is $0.235T_u$ under PGA = 0.8 g, showing a 6% reduction compared to the initial value. Under El-centro ground motion with PGA = 1.0 g, the maximum story drift reaches 1/75 rad, which

approaches the elastoplastic limit (1/50 rad). More details are shown in Table 5. At this moment, the maximum and minimum cable forces reach $0.302T_u$ and $0.237T_u$, respectively, indicating the variation of the cable force does not affect the self-centering performance of the PSCF. After the final loading, the performance-based design criteria, $M_d = 0.638M_{\text{IGO}} > 0.5M_{\text{IGO}}$, is satisfied and simultaneously, the anchorage and pretension measures are proved to be reliable.

The curves of the cable force versus gap-opening rotation under El-Centro seismic record with PGA = 1.0 g are shown in Fig. 28. As indicated in the figure, the curves of 4 PT strands of the second floor present a linear relation, while the curves of 4 PT strands of the first floor show a nonlinear relation due to factors such as the initial eccentricity, the installation deviation of the components, and the torsional effect of the beams when subjected to the lateral force. The variation of the cable force indicates a favorable self-centering performance of PSCF.

6.2.4. Strain condition

Table 6 lists the maximum strain of different parts of the testing substructure under two seismic ground motions with various magnitudes. It can be seen that the structure remain at an elastic state under PGA = 0.62 g. Under the seismic action of PGA = 0.8 g, plasticity firstly developed at the reinforcing plate with the maximum strain of 2641.03με under the action of seismic ground motion SH, and then appeared in the long beam portion flanges with the maximum strain of 1958.27με, which remained in the critical state of generating plasticity. Under the action of EL-Centro seismic record with PGA = 1.0 g, the maximum strain in the reinforcing plate increased to 3714.39με, and the strain in long beam portion flanges just exceeded 2000με as a result of the torsion effect due to lack of lateral restraint to the beam. It can be concluded that the strain development in the flange of column base, the reinforcing plate and the flange of frame beams is much faster than that in the rest locations of the structure. The time history curves of the

(a) Cable 17

(b) Cable 18

(c) Cable 19

(d) Cable 20

(e) Cable 29

(f) Cable 30
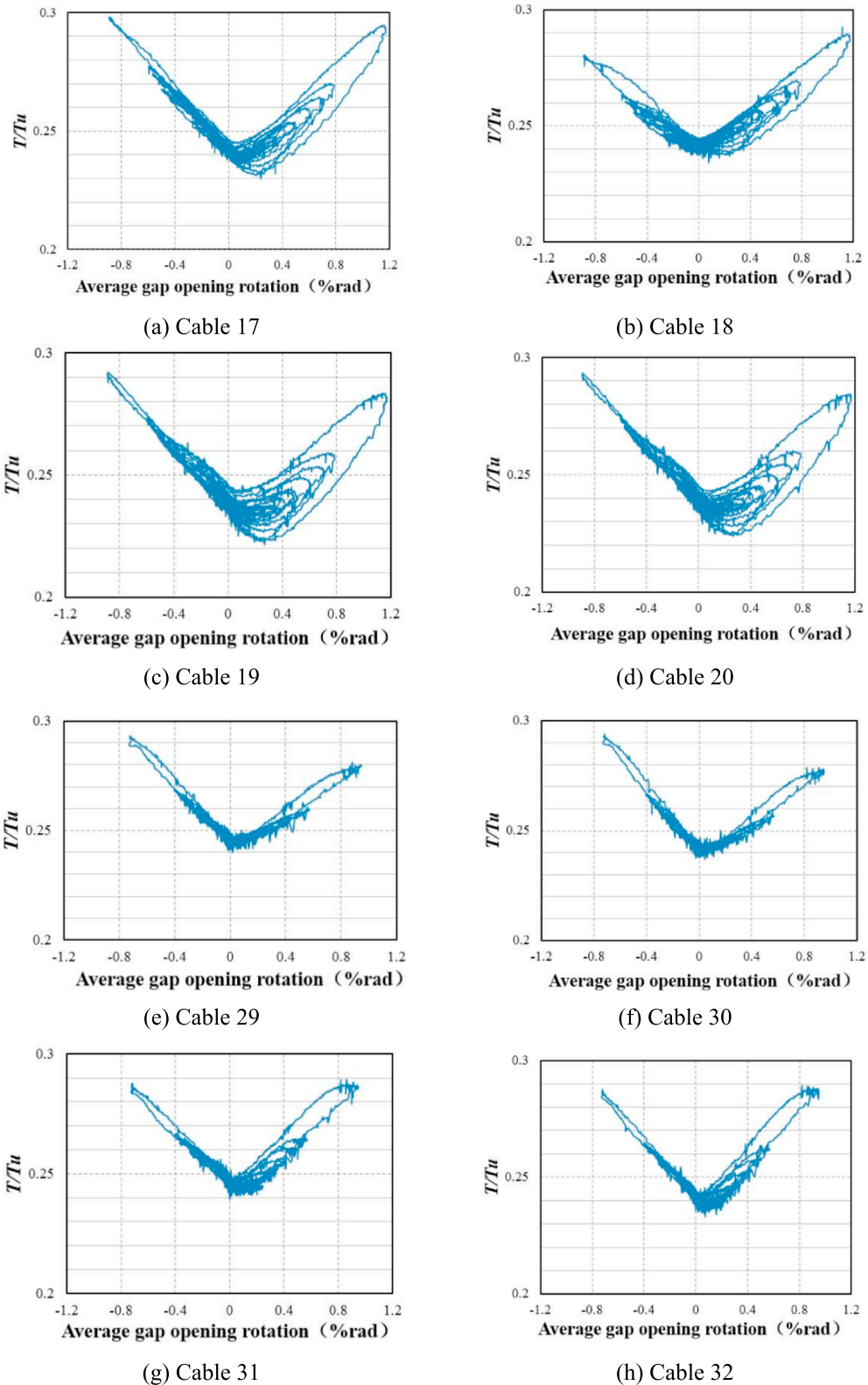
(g) Cable 31

(h) Cable 32

Fig. 28. PT force variation of the second floor under El-Centro with PGA = 1.0 g. (a) Cable 17. (b) Cable 18. (c) Cable 19. (d) Cable 20. (e) Cable 29. (f) Cable 30. (g) Cable 31. (h) Cable 32.

strain at various locations under EL-Centro seismic motion with PGA = 1.0 g are illustrated in Fig. 29, indicating that apparent plastic characteristic emerged in the reinforcing plates and the main components still remained an elastic state.

7. Quasi-static test

Since plasticity only developed in the reinforcing plate and the flanges of the long-beam portion after pseudo-dynamic test, quasi-static test was then conducted to investigate the seismic performance of PSCF

Table 6
Maximum strain at various positions under different earthquake magnitudes.

PGA	Seismic ground motion	Flanges of long-beam portion	Flanges of short-beam portion	Reinforcing plates	Web of the joint	Flanges of the joint	Webs of the column bases	Flanges of the column bases
0.62 g	EL	1629.8	822.4	1216.0	683.4	1216.0	618.3	1358.7
	SH	1706.1	840.3	1307.6	670.4	797.5	579.0	1366.5
0.8 g	EL	1759.9	898.6	2140.7	828.8	928.1	738.9	1615.6
	SH	1958.3	813.8	2641.0	1357.1	963.8	676.5	1615.2
1.0 g	EL	2124.7	1004.7	3714.4	989.6	1178.5	894.1	1850.6
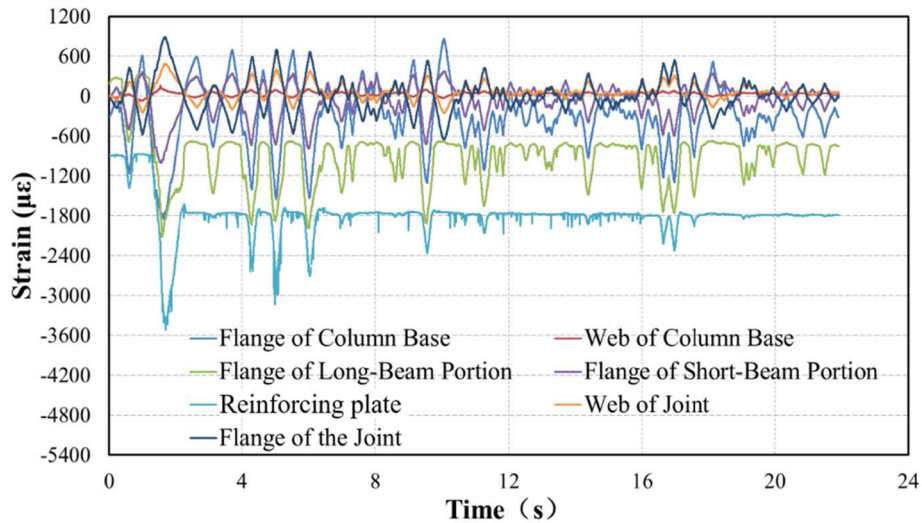
Fig. 29. Time history curves of the strain at various positions when PGA = 1.0 g.
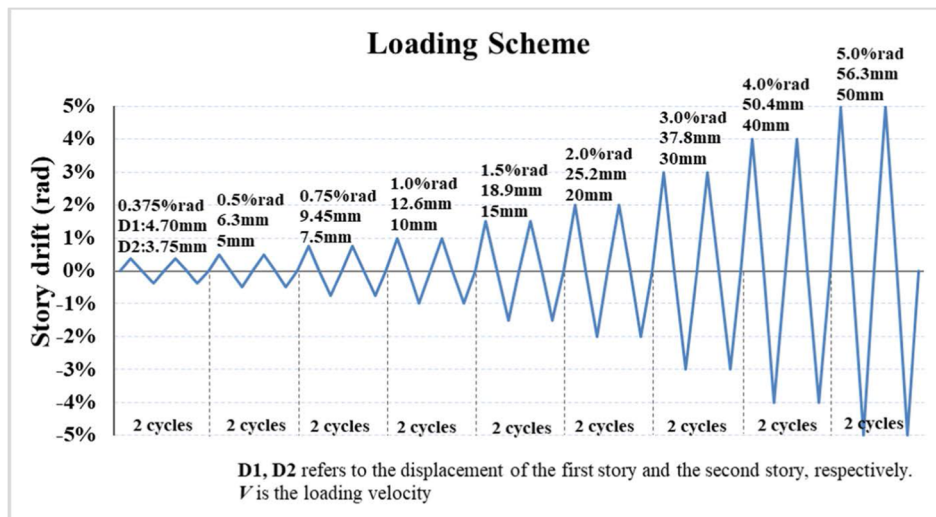
Fig. 30. Illustration of the loading scheme for quasi-static test.

under the condition of large deformation. By referring to the relevant requirements regarding the loading sequence of seismic test to the steel frame specified in AISC [28] and previous research [21], both the measured displacement and the story drift, were selected as the control parameters during the loading procedure. The loading sequence was divided into 9 loading steps. At the initial loading stage, the deformation remained at a low level and the loading frequency was controlled to be relatively high; with the increase of the loading step, the structural deformation kept increasing and the loading frequency was then adjusted to a relatively low level. Details of the loading scheme is illustrated in Fig. 30.

7.1. General test observations

As shown in Figs. 31–34, as the story drift (θ) increased from 0.375%rad to 0.5%rad, the whole structure remained in an elastic range without gap opening, and the lateral displacement of the structure was not obvious. Two sides of FC3 were selected to monitor the gap opening during the quasi-static test. When θ reached 0.75%, gap opening occurred and the maximum value was 0.82%rad in the first story. As θ increased to 2%rad, i.e., the elastoplastic limit for steel frame specified in Chinese *Code for Seismic Design of Buildings* [26], the deformation of the structure tended to be evident with the maximum gap opening of 2.32%rad, while no damage of components was

(a) θ=3%rad   (b) θ=5%rad
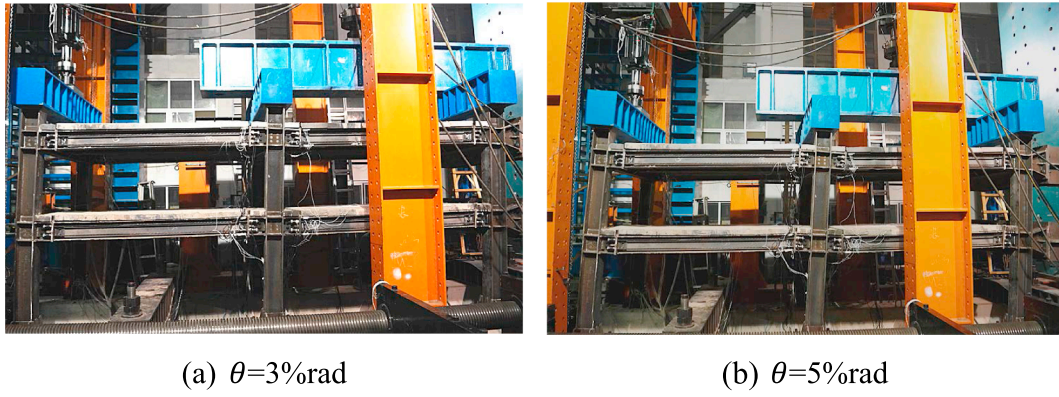
Fig. 31. Displacement of the testing substructure: (a) θ = 3%rad; (b) θ = 5%rad.

(a) θ=3%rad   (b) θ=4%rad   (c) θ=5%rad

Fig. 32. Gap opening: (a) θ = 3%rad; (b) θ = 4%rad; (c) θ = 5%rad.
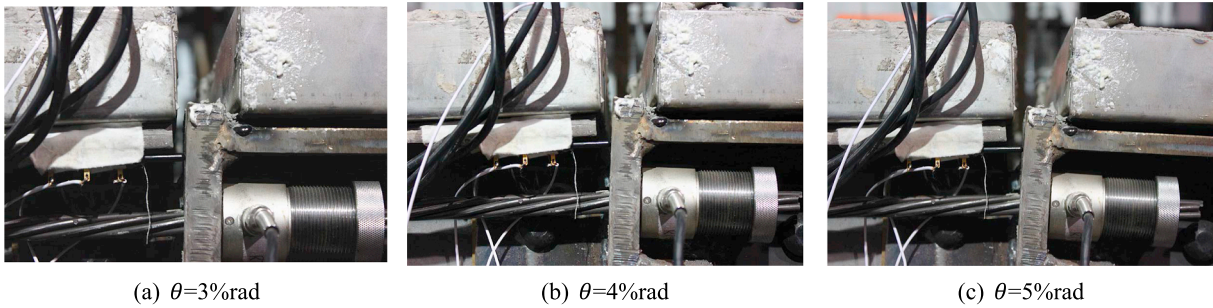
(a) θ=3%rad   (b) θ=4%rad   (c) θ=5%rad
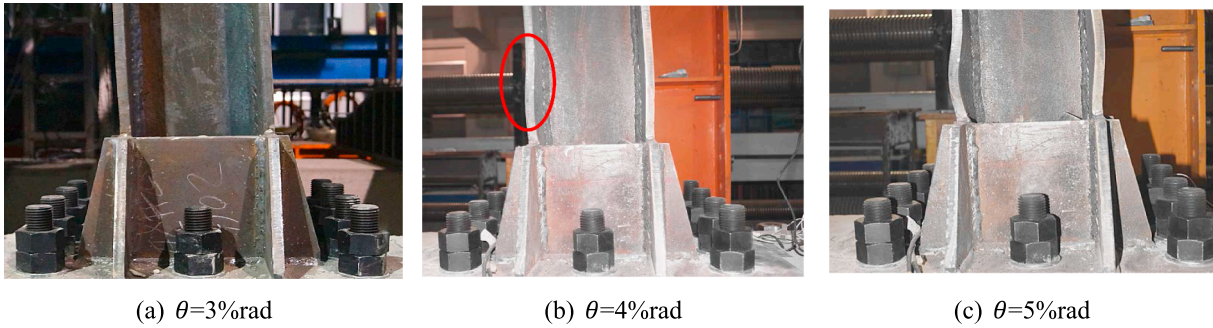
Fig. 33. Deformation of the column base: (a) θ = 3%rad; (b) θ = 4%rad; (c) θ = 5%rad.

(a) θ=3%rad   (b) θ=4%rad   (c) θ=5%rad
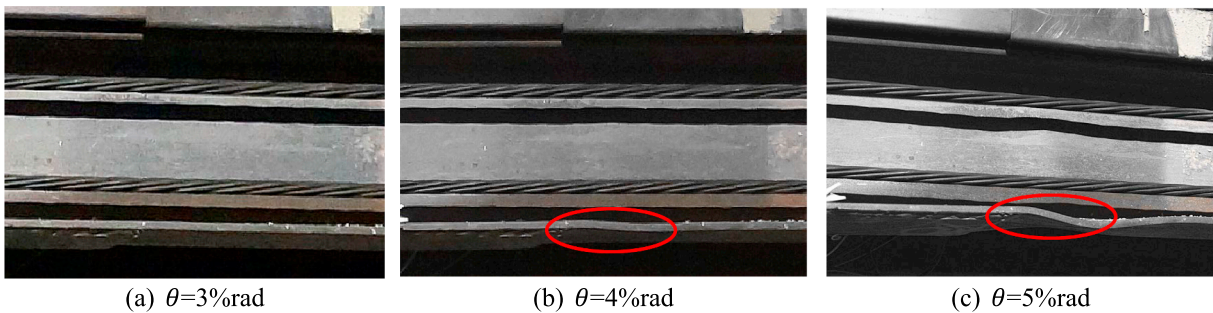
Fig. 34. Deformation of the long beam portion: (a) θ = 3%rad; (b) θ = 4%rad; (c) θ = 5%rad.

observed. When θ reached 3%rad, there was an evident lateral displacement with the gap opening of 3.79%rad. Bending deformation occurred at the column base due to the excessive lateral displacement of the frame while the long beam portion did not show any deformation. As θ increased to 4%rad, the gap opening increased to 5.47%rad, and the bottom flanges of the long beam portion as well as the flanges of the column foot buckled slightly. Lateral displacement was evident when θ

reached 0.05 rad, whereas the testing substructure still had a favorable performance without showing any decrease in structural capacity. After the final loading step, the lower flanges of the long beam portion buckled more evidently, and the buckling condition was extended to the beam web and the flanges of the column base distinctively. No local buckling was observed in the upper flanges of the beam due to the restraint function of the floor diaphragm.
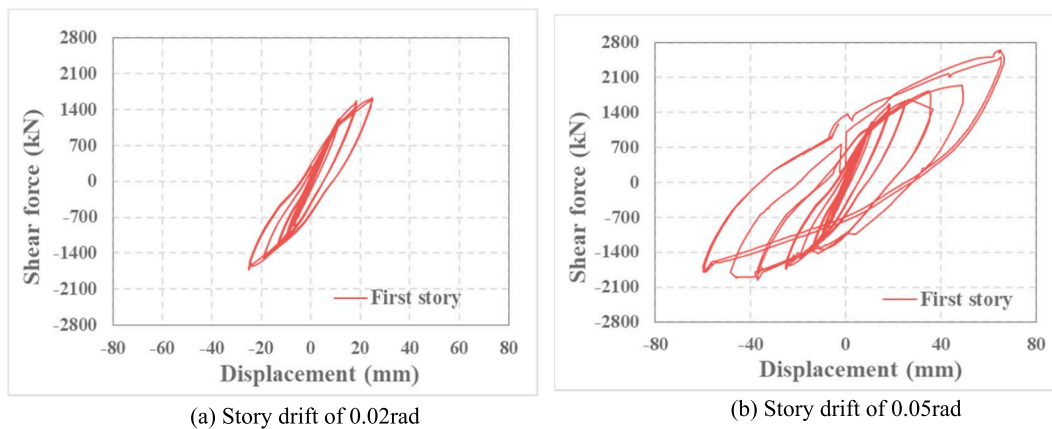
(a) Story drift of 0.02rad

(b) Story drift of 0.05rad

Fig. 35. Hysteretic curves for the first story of the testing substructure: (a) Story drift at 0.02 rad; (b) Story drift at 0.05 rad.

(a) Story drift of 0.02rad

(b) Story drift of 0.03rad

(c) Story drift of 0.04rad

(d) Story drift of 0.05rad
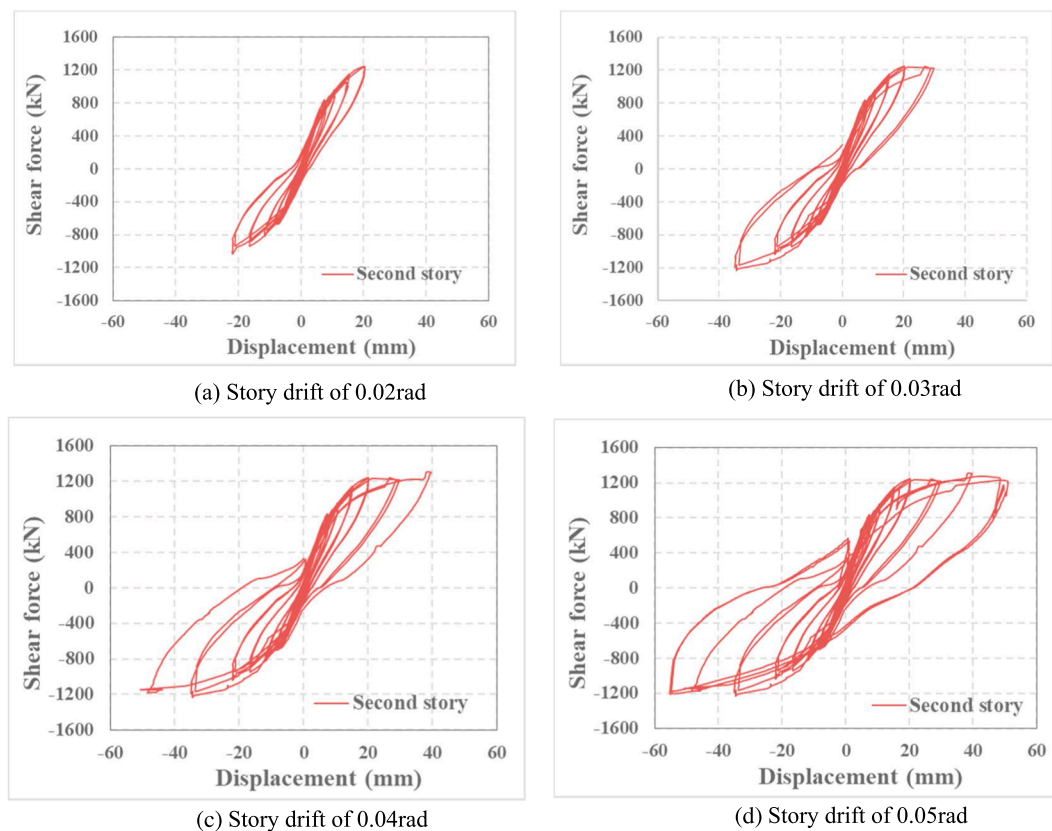
Fig. 36. Hysteretic curves for the second story of the testing substructure: (a) Story drift at 0.02 rad; (b) Story drift at 0.03 rad (c) Story drift at 0.04 rad (d) Story drift at 0.05 rad.

7.2. Hysteretic behavior

The base shear-displacement curves for the first story and the second story of the testing substructure under various loading levels are presented in Figs. 35 to 36. At the loading stage before 1.0%rad, the structure remains at an elastic stage with no gap opening occurring and the hysteretic curves present a linear state. When the story drift increases to 2%rad and 3%rad, the hysteretic curves for the first story of the testing substructure present to be in a shuttle shape due to the approximate rigid restraint of column base, which has caused the plastic development and affected the self-centering mechanism. For the second story, a typical double-flag shape of the hysteretic curves is shown at 2%rad, which has verified the self-centering character of the structure when the story drift reaches the elastoplastic limit under 8-

degree rare earthquakes specified in Chinese *Code for seismic design of buildings* [26]. Thereafter, hysteretic curves deviate from a flag shape due to excessive plastic deformation. When the story drift exceeds 3% rad in corresponding with extremely rare earthquakes, the hysteretic curves tend to be plumper and plumper due to the serious plasticity development.

Figs. 37 and 38 show the skeleton curves and the secant stiffness curves, respectively. The secant stiffness and the stiffness reduction are listed in Table 7. The skeleton curves of both stories had a linear relation and there was only slight decline for the secant stiffness at the initial loading stage. As θ increased from 0.75%rad to 2%rad, the curve slope gradually decreased and the secant stiffness was reduced by 38.93%. For the second story, the reduction of secant stiffness at 2%rad reached 52.43%, indicating the structural stiffness was impacted by the
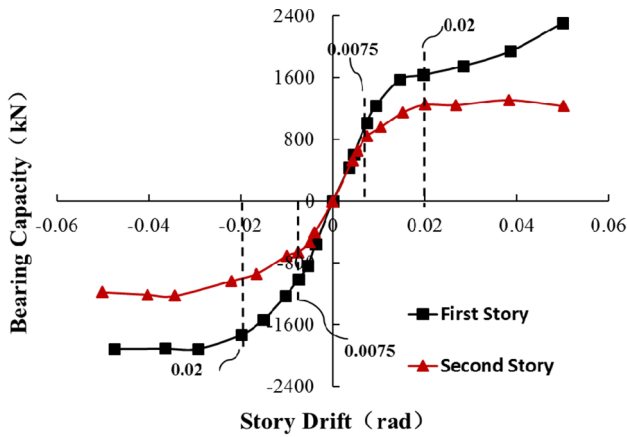
Fig. 37. Skeleton curves.
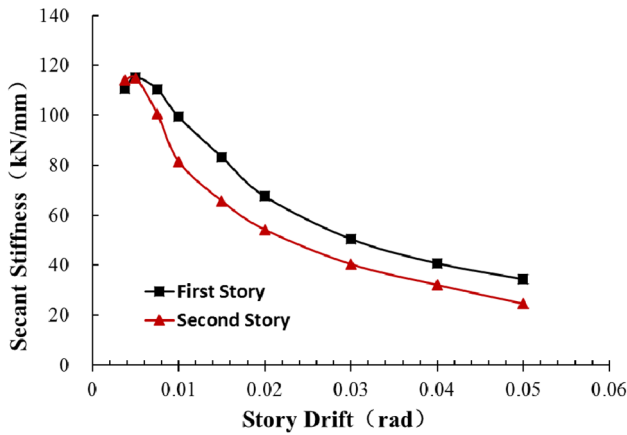
Fig. 38. Secant stiffness curves.

Table 7
Secant stiffness of structure (kN/mm).

θ (rad)	0.00375	0.0075	0.01	0.02	0.03	0.04	0.05
First story	110.6	110.4	99.4	67.5	50.5	40.7	34.4
Reduction	–	0.13%	10.13%	38.93%	54.36%	63.16%	68.88%
First story	114.1	100.7	81.5	54.3	40.4	32.1	24.6
Reduction	–	11.70%	28.53%	52.43%	64.58%	71.84%	78.47%

generation and development of the gap opening. When θ exceeded 0.02 rad, the variation of the structural stiffness tended to be smooth, where the maximum bearing capacity of the first story continued to

increase in positive direction of loading and stopped to increase in negative direction. While for the second story of the structure, the maximum bearing capacity stopped to increase in both directions. Under the condition of large structural deformation, i.e., when θ reached 4%rad and 5%rad, no decrease of the bearing capacity occurred though the column base and the beam buckled, indicating that PSCF had a favorable seismic performance.

7.3. Cable force

Eight strands of the SCB3 and SCB4 are selected to analyze the cable force variation, and their positions are shown in Fig. 27. The cable forces of the eight strands are shown in Table 8, where four strands installed on the inner side of two beams were selected to investigate the PT force-gap opening relation, as illustrated in Fig. 39.

As the story drift reached 0.03 rad, the maximum cable force reached 130.24kN ($0.5T_u$), the maximum reduction of cable force was 5.4% after the loading step and no buckling phenomenon was observed, indicating a favorable self-centering capacity of the PSCF. When the story drift increased to 0.04 rad, the maximum cable force reached 160.20kN ($0.62T_u$) and the maximum reduction of cable force reached 12.5% which occurred at the PT strand of the second floor at the end of this loading step. Local buckling at the long-beam portion may has some impact on maintaining the cable force in the strands. After this loading stage, the decompression moment M_d was 59% of the imminent gap-opening moment M_{IGO}, meeting the proposed design criteria of the PSC connection. When story drift reached 0.05 rad, the maximum cable force reached 172.23kN ($0.66T_u$), indicating that the steel strands had enough safe redundancy during this loading step. The local buckling condition in long-beam portions of second floor became more severe, the maximum reduction of cable force was 29.2% upon the quasi-static test. The decompression moment (M_d) was 17.88kN·m and the imminent gap-opening (M_{IGO}) was 33.14kN·m, still meeting the design criteria of $M_d = 0.54 M_{IGO} > 0.5M_{IGO}$. It can be concluded that the PSC connection had adequate self-centering capacity under large deformation conditions.

7.4. Strain condition

During the quasi-static test, strain development in typical parts of the testing substructure is monitored as shown in Fig. 40, where two dashed lines represent the yielding strain. When the story drift reached 1.5%rad, plasticity developed in the reinforcing plate, where the flange of the column base and the flange of the long beam portion were in the critical state. When the story drift reached 2%rad, the flange of the column base entered the plastic state. When the story drift increased from 3%rad to 4%rad, slightly buckling deformation generated at the column bases, for which the strain in the flange and the web exceeded

Table 8
PT force variation.

		Cable17 (kN)	Cable18 (kN)	Cable19 (kN)	Cable20 (kN)	Cable29 (kN)	Cable30 (kN)	Cable31 (kN)	Cable32 (kN)
Begin		64.8	66.08	62.54	63.31	64.37	63.68	63.19	61.81
0.03	Maximum	130.03	121.62	121.84	123.19	126.09	130.24	123.99	124.88
	End	65.23	67.15	63.63	63.07	61.82	60.84	59.78	58.99
	Delta	0.43	1.07	1.09	−0.24	−2.55	−2.84	−3.41	−2.82
		0.66%	1.62%	1.74%	−0.38%	−3.96%	−4.46%	−5.40%	−4.56%
0.04	Maximum	160.2	148.46	149.01	151.42	151.84	157.48	148.97	149.45
	End	63.93	65.11	61.76	61.58	58.1	56.82	58.32	55.35
	Delta	−0.87	−0.97	−0.78	−1.73	−6.27	−6.86	−4.87	−6.46
		−1.34%	−1.47%	−1.25%	−2.73%	−9.74%	−10.77%	−7.71%	−10.45%
0.05	Maximum	172.73	158.47	162.45	165.03	155.98	163.53	152.39	154.02
	End	60.17	59.78	60.42	59.78	46.84	45.07	47.21	45.5
	Delta	−4.63	−5.33	−1.34	−1.8	−11.26	−11.75	−11.11	−9.85
		−7.15%	−9.53%	−3.39%	−5.58%	−27.23%	−29.22%	−25.29%	−26.39%

(a) Cable 17

(b) Cable 19

(c) Cable 29

(d) Cable 31

Fig. 39. PT force of frame beams: (a) Cable 17; (b) Cable 19; (c) Cable 29; (d) Cable 31.
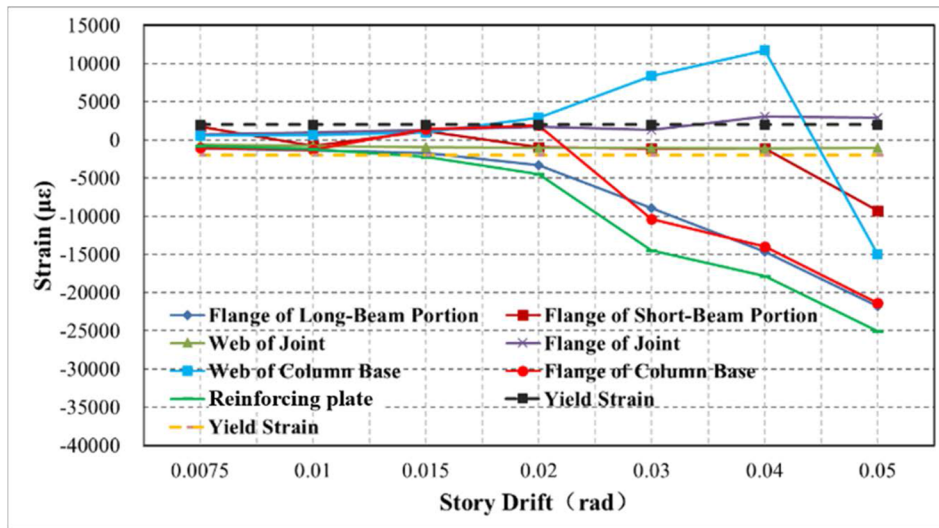
Fig. 40. Strain variation of typical position.

10000με, and the strain in long beam portion also exceeded 10000με. However, there was no visible deformation until the story drift of 5% rad, where buckling deformation generated in the flanges of both the column bases and the long-beam portions with the strain exceeding 20000με. Components were in the high strain state with the exception of the web of the joint, indicating that reinforcing plate had an outstanding performance in protecting the key zone from being damaged.

7.5. Performance of the floor system with the new type of the secondary beams

Displacement meters are set on each side of the SB1 and SB2 to investigate the slipping conditions and further to research the feasibility and reliability of the details of secondary beams. Fig. 41 shows the variation conditions of the slippages of both SB1 and SB2 (Δ') as well as the average gap opening (Δ) under various story drifts (θ_s). The slippage of secondary beams was mainly caused by the gap opening of the

(a) First story   (b) Second story
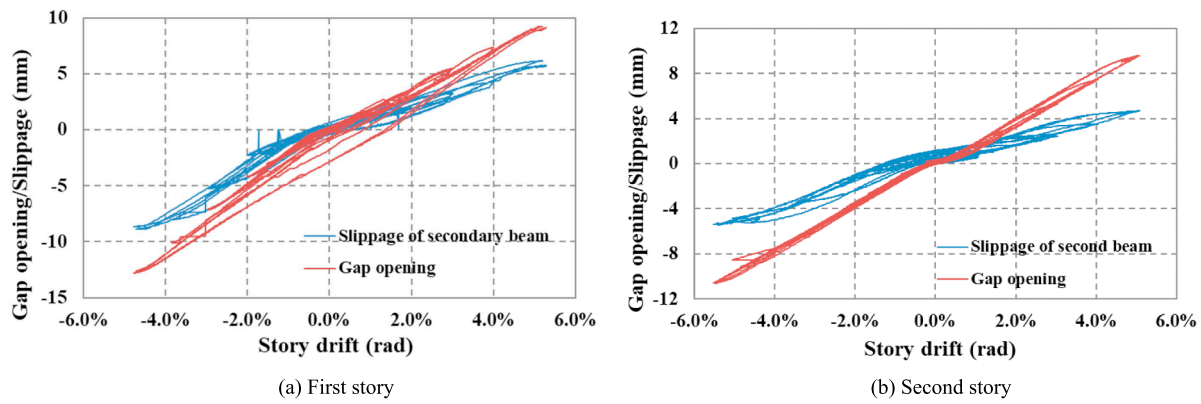
Fig. 41. Comparison of the sliding range and gap opening size: (a) First story; (b) Second story.

connection, where the gap opening of the connection increased more rapidly than the slippage of secondary beams with the same increment of story drift. When θ_s reached 0.75%rad, gap opening firstly generated and the secondary beam started to slip with the peak value of 0.52 mm, and meanwhile, the ratio of the maximum slippage of secondary beams and the average gap opening (Δ'/Δ) was 0.42. The value of Δ'/Δ increased with the increase of story drift before story drift of 5%rad. As story drift reached 4%rad, the maximum slippage of secondary beams (Δ') was 8 mm, which reached 79% of the average gap opening, revealing the fact that the slippage of secondary beams became smooth after overcoming the maximum static friction. Therefore, the new type of secondary beams achieved the target of enabling the gap opening of the structure and accommodating the expansion effect of PSCF. When story drift reached 5%rad, deformation of the whole structure became uncoordinated due to the excessive buckling in column base and beam, therefore, the working condition was no longer suitable for the new type of the secondary beam.

8. Conclusions

In this paper, experimental study on a 0.3 scaled, 2 × 2 bays, 2-story spatial prefabricated self-centering steel frame with web friction dampers (PSCF) has been carried out. Pseudo-dynamic test was performed to investigate the seismic performance of the frame under the action of several seismic ground motions. Quasi-static test was also conducted to investigate the mechanical performance of the frame under large deformation condition. A new floor slab system with sliding secondary beams has been proposed, and the gap-opening mechanism of the new system has been investigated and examined through the completed experiments. The following conclusions can be drawn:

(1) The spatial PSCF has a reliable self-centering mechanism. The structure was able to return to the initial position upon seismic actions with various magnitudes. During the pseudo-dynamic tests, the residual story drift and the residual gap opening remained at a relatively low level with the peak value reaching 0.106%rad and 0.077%rad, respectively. Before the story drift of 0.03 rad, a typical double-flag shaped hysteretic curves could be obtained for the second story of the structure, indicating that the spatial PSCF possesses favorable self-centering behavior under large deformation conditions.

(2) The adoption of web friction devices (WFDs) has effectively dissipated seismic energy and protected the main structure from being damaged. When story drift reached the elastoplastic limit (0.02 rad), only column base presented slight plastic development and the hysteretic curves became relatively plump due to the energy dissipation by WFDs. At the highest loading level with the story drift of 0.05 rad, only local buckling occurred at long-beam flange and column base. The whole structure still remained serviceable under extremely rare earthquakes, indicating that the web friction devices has effectively reduced the damage to the main components by dissipating seismic energy.

(3) The posttensioning and anchorage methods of steel strands were verified to be reliable to provide adequate self-centering capacity. At the loading stage with the story drift of 0.02 rad, the maximum reduction of posttensioned (PT) force of steel strands was within 5%. As the story drift reached 0.05 rad, only one certain steel strand exhibited about 30% PT force reduction due to the excessive local buckling of beam. For other steel strands, the PT force reduction still remained at a relatively low level. The PT force of all steel strands still satisfied the performance-based design criterion (i.e. $M_d > 0.5M_{IGO}$), indicating that the structure still had adequate safety margin to withstand multiple aftershocks under large deformation conditions.

(4) The new slab system with sliding secondary beams is able to accommodate the frame expansion and the gap-opening mechanism. As story drift reached 0.75%rad, gap opening firstly generated and the secondary beam started to slip. After overcoming the maximum static friction, gap opening and the slippage of secondary beams increases smoothly before 0.04 rad. Therefore, the new slab system has achieved the design objectives successfully.

(5) Testing results indicated that the proposed design targets were achieved successfully as follows: there was no gap opening and structural damage under frequent earthquakes; only slight gap opening and deformation occurred under fortification earthquakes and under rare and extremely rare earthquakes, gap opening occurred to dissipate energy and the whole structure still remained serviceable with only a few components buckling, indicating that the spatial PSCF possesses superior seismic behavior and deformation capacity.

References

[1] Ricles J, Sause R, Peng SW, Lu LW. Experimental evaluation of earthquake resistant post-tensioned steel connections. J Struct Eng 2002;128(7):850–9.
[2] Garlock M. Design, analysis, and experimental behavior of seismic resistant post-tensioned steel moment resisting frames. Bethlehem, Pennsylvania: Lehigh University; 2002.
[3] Garlock M, Ricles J, Sause R. Cyclic load tests and analysis of bolted top-and-seat angle connections. J Struct Eng 2003;129(12):1615–25.
[4] Garlock M, Ricles J, Sause R. Experimental studies on full-scale post-tensioned steel connections. J Struct Eng 2005;131(3):438–48.
[5] Mirzaie Aliabadi Mahbobeh, Bahaari Mohammad Reza, Torabian Shahabeddin. Design and analytical evaluation of a new self-centering connection with bolted T-stub devices. Adv Mater Sci Eng Volume 2013;Article ID 163021, 12 pages.
[6] Wang W, Fang Ch, Liu J. Self-centering beam-to-column connections with combined superelastic SMA bolts and steel angles. Struct Eng 2017;143(2):04016175.
[7] Kim H, Christopoulos C. Friction damped post-tensioned self-centering steel moment-resisting frames. J Struct Eng 2008;134(11):1768–79.
[8] Rojas P, Ricles JM, Sause R. Seismic performance of post-tensioned steel moment

resisting frames with friction devices. J Struct Eng 2005;131(4):529–40.

[9] Wolski M, Ricles M, Sause R. Experimental study of a self-centering beam-column connection with bottom flange friction device. J Struct Eng 2009;135(5):479–88.

[10] Iyama J, Seo CY, Ricles JM, Sause R. Self-centering MRFs with bottom flange friction devices under earthquake loading. J Constr Steel Res 2009;65:314–25.

[11] Lin YC, Sause R, Ricles J. Seismic performance of a large-scale steel self-centering moment-resisting frame: MCE hybrid simulations and quasi-static pushover tests. J Struct Eng 2013;139(7):1227–36.

[12] Lin YC, Sause R, Ricles J. Seismic performance of steel self-centering moment-resisting frame: hybrid simulations under design basis earthquake. J Struct Eng 2013;139(11):1823–32.

[13] Ramhormozian S, Clifton GC, Maetzig S, Cvitanich D. Influence of the Asymmetric Friction Connection (AFC) ply configuration, surface condition, and material on the AFC sliding behaviour. In: New Zealand Society for Earthquake Engineering (NZSEE) Annual Technical Conference 2016: Christchurch, New Zealand.

[14] Ramhormozian S, Clifton GC, Maetzig S, Davet Cvitanich D. Stiffness-based approach for Belleville springs use in friction sliding structural connections. J Constr Steel Res 2017;138:340–56.

[15] Garlock M, Sause R, Ricles J. Behavior and design of posttensioned steel frame systems. J Struct Eng 2007;133(3):389–99.

[16] Garlock M, Li J. Steel self-centering moment frames with collector beam floor diaphragms. J Constr Steel Res 2008;64(5):526–38.

[17] Chou CC, Wang YC, Chen JH. Seismic design and behavior of post-tensioned steel connections including effects of a composite slab. Eng Struct 2008;30:3014–23.

[18] Chou CC, Tsai K, Yang WC. Self-centering steel connections with steel bars and a discontinuous composite slab. Earthquake Eng Struct Dyn 2009;38:403–22.

[19] Kim HJ, Christopoulos C. Seismic design procedure and seismic response of post-tensioned self-centering steel frames. Earthquake Eng Struct Dyn 2009;38:355–76.

[20] Huang XG, Zhou Z, Xie Q, Xue RL, Zhu DP. Force distribution analysis of self-centering coupled-beams for moment-resisting-frames without floor elongation.

Eng Struct 2017;147:328–44.

[21] Zhang AL, Zhang YX, Li R, Wang ZY. Cyclic behavior of a prefabricated self-centering beam–column connection with a bolted web friction device. Eng Struct 2016;111:185–98.

[22] Zhang YX, Ye JJ, Yang F, Chen YY. Dynamic behavior and time-history analysis of integral self-centering moment resisting frames. China Civil Eng J 2015;48(7):30–40. [in Chinese].

[23] Zhang YX, Zhang AL, Sun WL. Behavior study of self-centering beam-column connections in resilient steel frames after earthquake. Indus Constr 2014;44(502):160–7. [in Chinese].

[24] Zhang AL, Zhang YX, Zhao W, Fei CC. Pseudo dynamic test study of resilient prefabricated prestressed steel frame. J Vib Shock 2016;35(5):207–15. (in Chinese).

[25] Zhang YX, Wang ZY, Zhao W, Zhao WZ. A pseudo-dynamic test study on a self-centering prefabricated steel frame with a column base connected by semi-rigid joints. Advanced Steel Construction 2016;12(3):296–315.

[26] GB 50011-2010 (2016), Code for seismic design of buildings. Beijing: China Architecture & Building Press; 2016. [in Chinese].

[27] Fan YL, Guo YR, Xia Y, He WH. Remote collaborative pseudo dynamic test on multistory frame. China Civil Eng J 2011;2:28–35. [in Chinese].

[28] ANSI/AISC. Seismic provisions for structural steel buildings. Chicago (IL): American Institute of Steel Construction; 2005.

[29] JGJ82-2011, Technical Specifications for high strength bolt connections of steel structures. Beijing: China Architecture & Building Press. [in Chinese].

[30] Zhang YX, Zhang HX, Liu AR, Li ZX. Performance-based design research of resilient prefabricated prestressed steel frames. Progr Steel Build Struct 2017;19(4):1–9. [in Chinese].

[31] Zhang YX, Zhao WZ, Chen YY, Ning G. Experimental research of slotted bolted friction device. Earthq Resistant Eng Retrofitting 2015;37(4):90–5. [in Chinese].

[32] GB50068-2001. Unified Standard of Reliability Design for Building Structures. Beijing: China Architecture & Building Press. [in Chinese].